A description of turbulent wall-flow vorticity consistent with mean dynamics

J. C. Klewicki†

Department of Mechanical Engineering, University of Melbourne, Melbourne, VIC 3010, Australia
Department of Mechanical Engineering, University of New Hampshire, Durham, NH 03824, USA

A depiction of the mean and fluctuating vorticity structure in turbulent wall flows is presented and described within the context of the self-similar properties admitted by the mean dynamical equation. Data from a relatively wide range of numerical and physical experiments are used to explore and clarify the structure postulated. The mean vorticity indicator for the onset of the four-layer regime of the mean dynamics is revealed. With increasing Reynolds number, the mean vorticity is shown to segregate into two increasingly well-defined domains. Half of the mean vorticity concentrates into a near-wall region of width (relative to the overall flow width) that diminishes proportionally to the inverse square root of Reynolds number. The remainder of the mean vorticity is spread, with diminishing amplitude, over an outer domain that approaches the overall flow width at high Reynolds number. Vorticity stretching and reorientation are surmised to be the characteristic mechanisms accounting for the inner domain behaviour of both the mean and fluctuating vorticity. Vorticity dispersion via advective transport is surmised to be the characteristic mechanism in the outer domain. In this domain, the fluctuating enstrophy approaches that of the instantaneous enstrophy with increasing Reynolds number. This underpins an emerging self-similarity between the mean and r.m.s. vorticity in the domain where the mean velocity profile is logarithmic. The Reynolds number dependence of a number of properties associated with the vorticity field is explored and quantified. The study closes with brief account of the combined vortical and mean dynamical structure of turbulent wall flows.

Key words: turbulence theory, turbulent flows, turbulent boundary layers

1. Introduction

The condition of non-zero vorticity is a definitional feature of wall-bounded flows. For this reason, vorticity has long been purported to be the *natural* variable for studying these flows, e.g. Lighthill (1963). In the turbulent wall flows under investigation, the component of vorticity parallel to the wall and perpendicular to the direction of the main flow (hereafter, called the spanwise component) is the only one with a non-negligible mean value. This mean vorticity is well-approximated by the wall-normal derivative of the mean velocity, and thus describes the increments in mean velocity (circulation per unit length, Γ) required to reconcile the free-stream flow with

† Email address for correspondence: joe.klewicki@unh.edu

a no-slip wall. Such properties connect the structure of the vorticity and momentum fields.

Recent studies reveal that the mean dynamical equations for the canonical wall flows admit an invariant form (Wei *et al.* 2005; Fife *et al.* 2005*a*; Fife, Klewicki & Wei 2009; Klewicki, Fife & Wei 2009). This underlies a similarity solution to these equations over a well-defined interior domain (Klewicki 2013*a*). Herein, turbulent wall-flow vorticity characteristics are described in a manner that is consistent with this similarity solution, and other properties admitted by the mean momentum equation.

We consider statistically stationary, fully developed, incompressible turbulent flow in pressure-driven pipes and planar channels, and in the developing zero-pressure-gradient boundary layer. The main flow is in the *x*-direction, with the wall-normal direction denoted by y ($=\delta - r$ in the pipe, where δ denotes the pipe radius). Upper-case letters or angle brackets denote time-averaged quantities. Lower-case letters indicate fluctuations about the mean, and instantaneous quantities are denoted by a tilde. The x, y and z (x, r, θ) velocity components are given by variants of u, v and w respectively. Vorticity component directions are denoted by their subscript, and δ is used to indicate the boundary layer thickness, pipe radius, or half channel height. A superscript '+' denotes normalization by the kinematic viscosity, ν, and the friction velocity, $u_\tau = \sqrt{\tau_w/\rho}$, where ρ and τ_w are the mass density, and mean wall shear stress, respectively. The Reynolds number is given by $\delta^+ = \delta u_\tau/\nu = 1/\epsilon^2$. The value of the circulation per unit length integrated to the free stream or centreline is denoted by Γ_e.

1.1. *Transitional regime*

Fully developed laminar Poiseuille flows are dynamically characterized by a balance between a driving pressure force and a retarding viscous force. The dynamics of the laminar boundary layer are dictated by a retarding viscous force that affects a time rate of change of streamwise momentum. At sufficiently high Reynolds numbers, these flows develop instabilities, and the inertia of the turbulence becomes significant, both instantaneously and as a mean dynamical effect. In the transitional regime turbulent inertia drives the rapid redistribution of the mean momentum. During this process, the relative magnitudes of the terms in the mean dynamical equation qualitatively change (Elsnab *et al.* 2011; Klewicki, Ebner & Wu 2011; Klewicki *et al.* 2012; Sayadi, Hamman & Moin 2013), culminating with the establishment of the four-layer structure first revealed by Wei *et al.* (2005). In the pipe and channel, $\delta^+ \simeq 180$ marks the onset of the four-layer regime, while this onset occurs at $\delta^+ \simeq 370$ in the boundary layer (Elsnab *et al.* 2011; Klewicki *et al.* 2011, 2012). Properties of the four layers are summarized in table 1.

In each of the subject flows the mean vorticity, Ω_z, undergoes developments commensurate with the dynamical processes just described. Wallward momentum transport occurs simultaneously with outward vorticity transport, as these are governed by the same physical mechanisms (Klewicki *et al.* 2007; Eyink 2008). Self-sustaining vorticity stretching and reorientation mechanisms initiate and intensify during the transitional regime. These lead to the concentration of $\sim 1/2$ of the total Ω_z within a region adjacent to the surface that has a width that decreases relative to δ like $1/\sqrt{\delta^+}$ (Wei *et al.* 2005; Klewicki *et al.* 2007; Elsnab *et al.* 2011; Klewicki *et al.* 2011, 2012). The remainder of the Ω_z is then spread over a domain whose width approaches δ as $\delta^+ \to \infty$. These mechanisms, which are responsible for the eventual development of a logarithmic mean velocity profile, initiate during the transitional regime. Morrill-Winter & Klewicki (2013) also provide evidence that these two regions of the Ω_z

Physical layer	Magnitude ordering (pipe & channel)	Magnitude ordering (boundary layer)	Δy increment	$|\Delta \Gamma|$ increment
I	$|PG| \simeq |VF| \gg |TI|$	$|MI| \simeq |VF| \gg |TI|$	$O(\nu/u_\tau)$ $(\leqslant 3)$	$O(u_\tau)$ $(\leqslant 3)$
II	$|VF| \simeq |TI| \gg |PG|$	$|VF| \simeq |TI| \gg |MI|$	$O\left(\sqrt{\nu\delta/u_\tau}\right)$ $(\simeq 1.6)$	$O(U_e)$ $(\simeq 0.5)$
III	$|PG| \simeq |VF| \simeq |TI|$	$|MI| \simeq |VF| \simeq |TI|$	$O\left(\sqrt{\nu\delta/u_\tau}\right)$ $(\simeq 1.0)$	$O(u_\tau)$ $(\simeq 1)$
IV	$|PG| \simeq |TI| \gg |VF|$	$|MI| \simeq |TI| \gg |VF|$	$O(\delta)$ $(\rightarrow 1)$	$O(U_e)$ $(\rightarrow 0.5)$

TABLE 1. Magnitude ordering and scaling behaviours associated with the four layer structure of (1.1). Note that U_e equals U_∞ in the boundary layer and U_c in the pipe and channel (Wei *et al.* 2005; Fife *et al.* 2009). *PG*, *VF*, *MI* and *TI* respectively refer to the mean pressure gradient, mean viscous force, mean flow inertia and mean effect of the turbulent inertia terms in the mean momentum equation.

profile are associated with two different mechanisms for scale separation between the sizes of the motions characteristic of the velocity and vorticity fields, respectively. Here we show that the outer region mechanism becomes distinct at the onset of the four-layer regime, and provide evidence that it gives rise to an outer flow comprised of approximately uniform-momentum zones as first revealed by Meinhart & Adrian (1995), segregated by narrow strips of elevated vorticity that Priyadarshana *et al.* (2007) called *vortical fissures*, also see Adrian, Meinhart & Tomkins (2000) and Morris *et al.* (2007).

1.2. *Four-layer regime*

In the four-layer regime, the mean dynamical equations admit invariant forms that determine the scaling behaviours of their solutions. With increasing δ^+, these scaling behaviours become increasingly well-established (Wei *et al.* 2005; Fife *et al.* 2005*a*, 2009; Klewicki *et al.* 2009; Klewicki 2013*a*). Consider, for example, the inner-normalized mean momentum equation for the turbulent boundary layer,

$$\left(U^+\frac{\partial U^+}{\partial x^+} + V^+\frac{\partial U^+}{\partial y^+}\right) - \frac{\partial T^+}{\partial y^+} = \frac{\partial^2 U^+}{\partial y^{+2}}, \tag{1.1}$$

where $T^+ = -\langle uv\rangle^+$. Mean inertia (*MI*) is represented by the terms involving mean velocity on the left. The remaining term on the left is the mean effect of turbulent inertia (*TI*). The term on the right of (1.1) is the mean viscous force (*VF*). The corresponding pipe and channel flow equations are similar, but the *MI* term is replaced by a mean pressure gradient term, *PG*, that at any given δ^+ is everywhere equal to $1/\delta^+ = \epsilon^2$. Given the mean momentum equation, remarkably little else is required to analytically determine the layer scaling properties, to within $O(1)$ coefficients, indicated in table 1. The existence and properties of layer I are derivable from a Taylor series at the wall. The properties of layers II–IV require the existence of a region away from the wall where the leading-order balance is $MI - TI = 0$, and a region near the wall where $TI + VF = 0$. All the rest is determinable from analysis of the mean momentum equation and its boundary conditions, e.g. Fife *et al.* (2005*a*, 2009).

Note also that

$$TI = \frac{\partial T^+}{\partial y^+} = -\frac{\partial \langle uv\rangle^+}{\partial y^+} = \langle v\omega_z\rangle^+ - \langle w\omega_y\rangle^+ + \frac{\partial}{\partial x^+}\left(\langle v^2\rangle^+ + \langle w^2\rangle^+ - \langle u^2\rangle^+\right). \tag{1.2}$$
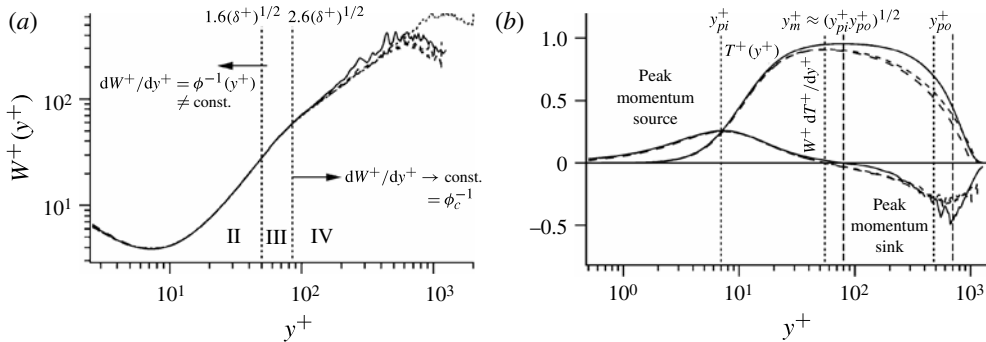
FIGURE 1. (a) Distribution $W^+(y^+)$ for pipe, channel, and boundary layer flows: pipe flow DNS of Wu & Moin (2008) at $\delta^+ = 1142$ (- - -); boundary layer DNS of Schlatter & Orlu (2010) at $\delta^+ = 1245$ (——); channel flow DNS of Abe, Kawamura & Matsuo (2004) at $\delta^+ = 1020$ (– – –); channel flow DNS of Hoyas & Jimenez (2006) at $\delta^+ = 2004$ (· · · · ·). Vertical lines denoting the beginning and end of layer III are computed for $\delta^+ = 1000$ (see table 1). (b) Distributions of $T^+ = -\overline{uv}^+$ and $W^+ dT^+/dy^+$ versus y^+ for pipe, channel and boundary layer flows. Vertical lines are associated with the pipe and channel (dotted) and boundary layer (dashed) profiles, respectively. Pre-multiplication of dT^+/dy^+ by W^+ reveals the mean source/sink balance associated with *TI*. Note that *W* attains its minimum and maximum at $y = y_{pi}$ and $y = y_{po}$, respectively. Line styles are the same as in (a).

The last term in (1.2) is identically zero in channel and pipe flow, and negligible under the boundary layer approximation. Thus, the *TI* term is well-approximated by the difference of the indicated velocity–vorticity correlations, especially as $\delta^+ \to \infty$.

The mean momentum equations for the canonical turbulent wall flows, including (1.1), admit similarity solutions (Klewicki 2013a). Accordingly, a coordinate stretching function ensures that a single self-similar solution holds as δ^+ is varied. This coordinate stretching function is denoted by ϕ, and is defined by

$$\frac{dW}{dy} = \phi^{-1}, \tag{1.3}$$

where $W^+(y^+)$ (shown for different δ^+ wall flows in figure 1a) is the continuous distribution of widths of a hierarchy of scaling layers called the L_β hierarchy, e.g. Fife *et al.* (2009) and Klewicki (2013a). $W^+(y^+)$ is formally related to the decay rate of the *TI* term in (1.1). Generally, however, W^+ is most accurately computed using $W^+ = (-\partial^2 U^+/\partial y^{+2})^{-1/2}$. Physically, at any location on the L_β hierarchy *W* is the mean length scale of the inertial turbulent motions that transport momentum. Conceptually, *W* is similar to von Kármán's representation of Prandtl's mixing length (von Kármán 1930). His formulation, however, stems from an intuited similarity hypothesis, while the properties of $W(y)$ are determined from an analysis of the mean dynamical equation. Specifically, normalization of the mean momentum equation using u_τ and *W* formally yields a single invariant form that holds over the domain where the *TI* term is a decreasing function of *y*, i.e. on the domain of the L_β hierarchy. This domain extends from $y^+ = y_{pi}^+ \simeq 7$ to $y/\delta = y_{po}/\delta \simeq 0.5$, or equivalently between the peak momentum source and sink locations in figure 1(b) (Fife *et al.* 2009; Klewicki *et al.* 2011).

The position, y_m^+, where $T^+ = -\langle uv \rangle^+$ attains its maximum (zero crossing of *TI*) is always located in layer III. Across layer III, the layer II mean force balance is broken,

and exchanged for the balance that emerges in layer IV (table 1). The analysis shows that this same balance breaking and exchange of mean forces is replicated across every layer (of width $W(y)$) of the L_β hierarchy, and thus occurs as a function of y. The cumulative effect of these processes on the hierarchy give rise to the layer structure listed in table 1. Layer III is therefore appropriately viewed as the central layer in the hierarchy, since, in fact, its scaling properties derive from the underlying ensemble of layers. For this reason y_m^+ is well-approximated by $(y_{pi}^+ y_{po}^+)^{1/2}$ (figure 1b).

The function ϕ describes the rate at which y varies relative to the local mean size of the inertial motions responsible for turbulent momentum transport. This is exemplified by figure 1(b), which shows that when the *TI* term in (1.1) is weighted by $W^+(y^+)$ and plotted on a log scale, its source and sink contributions become symmetrically distributed about its zero-crossing (maximum in T^+). This is a consequence of the turbulent motions increasing in scale approximately in proportion to y, as reflected by the W^+ profile (figure 1a). The decay rate of the *TI* function between y_{pi} and y_{po} determines the behaviour of W^+ (Fife *et al.* 2005b, 2009).

The framework used herein derives from the magnitude ordering of terms in (1.1). From the resulting four-layer structure (table 1), it is apparent that the coordinate stretching, ϕ, is operative over regions of the flow where the mean dynamics are governed by differing sets of leading-order terms. Specifically, the *VF* term loses leading-order across layer III, and here there is also a corresponding change in the qualitative behaviour of ϕ. As depicted in figure 1(a), ϕ is well-approximated by a non-constant $O(1)$ function of y^+ on the wallward side of layer III. Beyond layer III, ϕ is increasingly well-approximated by an $O(1)$ constant, $\phi = \phi_c$, as $\delta^+ \to \infty$. The relative simplicity of the outer ($\phi = \phi_c$) self-similarity leads to an explicit closure of (1.1) on a subdomain between the outer edge of layer III and $y_{po}/\delta \simeq 0.5$ (Klewicki 2013a). By exploiting the invariant form of (1.1), one can develop an independent differential relationship between U^+ and T^+ (Fife *et al.* 2005b, 2009; Klewicki *et al.* 2009; Klewicki 2013a). As $\delta^+ \to \infty$, the outer similarity solution emerges in concert with the more slowly developing inner self-similarity ($\phi \neq$ const.) that is operative between $y_{pi}^+ \simeq 7$ and the outer edge of layer III ($y^+ \simeq 2.6\sqrt{\delta^+}$, or equivalently, $\epsilon y^+ = 2.6$). These behaviours exist for all of the canonical wall flows (Klewicki 2013a).

As shown in figure 2, the inner and outer self-similar domains respectively coincide with where the $\langle w\omega_y \rangle$ contribution to *TI* becomes dominant over $\langle v\omega_z \rangle$ ($y < y_m$), and where the $\langle v\omega_z \rangle$ contribution becomes dominant over $\langle w\omega_y \rangle$ ($y > y_m$). These contributions are associated with the spatial confinement and spatial dispersion mechanisms of scale separation described by Morrill-Winter & Klewicki (2013) and depicted in figure 3.

1.3. *Physical model*

The primary aim of this study is to describe and explain a body of results that collectively support the depiction of the turbulent wall-flow vorticity field given in figure 3. Figure 3 was constructed by considering what the momentum equation analyses just described indicate about the structure and scaling properties of the vorticity field, as well as the physical mechanisms that underlie this structure.

The singular limit of the boundary layer is often conceptualized as a differentially thin vortex sheet that has a circulation per unit length of Γ_e. For both laminar and turbulent boundary layers, this limit is approached because the relative size of the domain where the viscous force has leading order diminishes as $\delta^+ \to \infty$. For fixed ν, the limit $\delta^+ \to \infty$ can generically be obtained by two separate means: $|\Gamma_e| \to \infty$
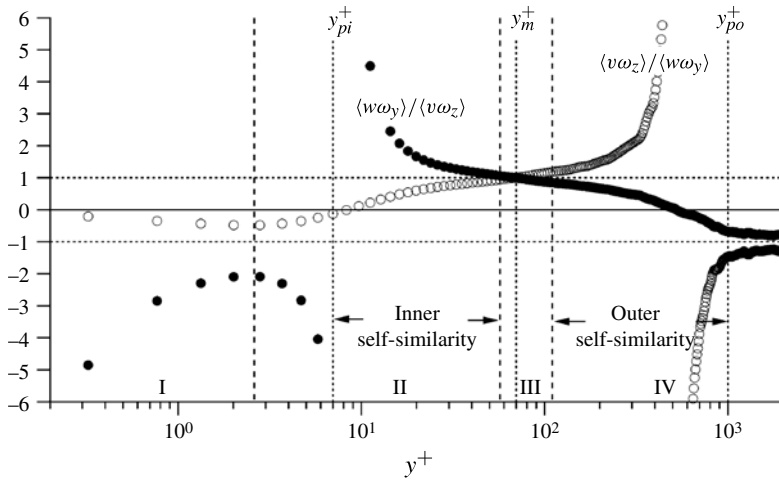
FIGURE 2. Ratios of the velocity vorticity correlations in (1.2) versus y^+. Vertical dashed lines denote the boundaries of layers I–IV. Vertical dotted lines denote the upper and lower boundaries of the self-similar regions associated with the coordinate stretching function ϕ, and the geometric centre, y_m^+, which is also the zero-crossing of *TI*. Data are from the $\delta^+ = 2004$ channel flow DNS of Hoyas & Jimenez (2006).
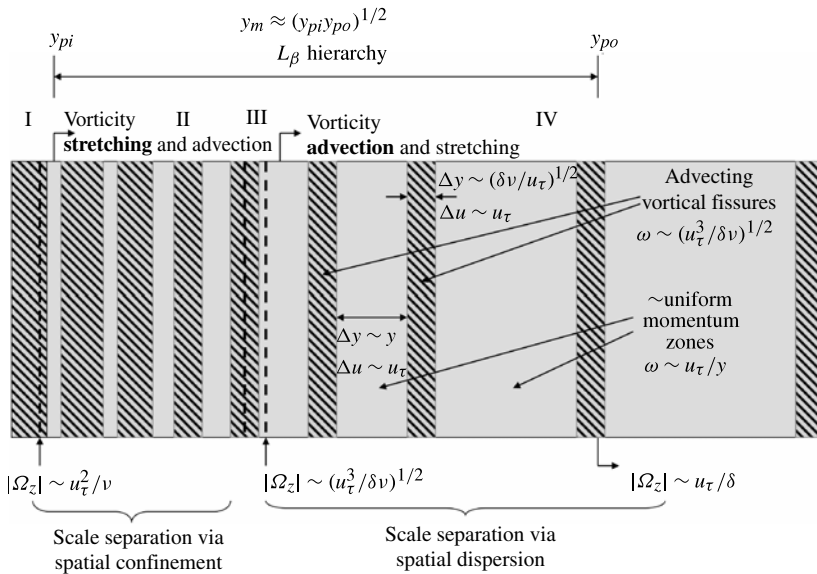

FIGURE 3. Schematic depiction of the vorticity field attributes in turbulent wall flows. The dominant processes responsible for scale separation between the velocity and vorticity fields change across layer III. The velocity field motions (light grey) are space-filling throughout the flow. The vorticity field motions (hatched regions) are confined to a sub-volume near the wall via vorticity stretching, and then the resulting thin regions of concentrated vorticity, *vortical fissures*, are dispersed by advective transport over the volume of layer IV. Note that for clarity the horizontal scale is stretched, e.g. layer II is actually only ~ 1.6 times wider than layer III, see table 1.

for fixed δ, and $\delta \to \infty$ for fixed $|\Gamma_e|$. In the first case, the domain size is fixed and the region of non-negligible viscous force diminishes in physical space. In the second case, both the overall domain size and the viscous region increase in physical space, but the growth of the domain size out-paces that of the viscous region. By definition, a similarity solution results from a parameter-free invariant form of the governing equation. Thus, for example, ϕ is analogous to the $y/x \sim Re_x^{-1/2}$ coordinate stretching associated with the similarity solution of the laminar boundary layer equation, as both describe the rate at which the region of non-negligible viscous force diminishes relative to the overall size of the flow domain (Klewicki 2013*b*).

In reference to the momentum transport associated with the vortical fissures of figure 3, Priyadarshana *et al.* (2007) revealed that the cospectral contributions underlying $\langle v\omega_z \rangle$ are associated with *scale selections*. Here the predominant contributions to the cospectra are centred about the peak in the v spectra, or the peak in the ω_z spectra, or both, in contrast to concentrating in the wavenumber range where the two spectra overlap. The scale selection about the peak in the ω_z spectrum is readily conceptualized as pertaining to the velocity fluctuations local to an intense vortical motion. In the context of the structure revealed by Meinhart & Adrian (1995), Priyadarshana *et al.* (2007) postulated that the scale selection associated with v derives from the advective meandering of the vortical fissures through the low-level vorticity of the uniform-momentum zones. Consistent with the depiction of figure 3, Morrill-Winter & Klewicki (2013) found that for $1500 \lesssim \delta^+ \lesssim 890\,000$ the v scale selection dominates the cospectrum starting near the outer edge of layer III, while both v and ω_z scale selections are present in layer II.

Morrill-Winter & Klewicki (2013) also provide evidence that the physical processes underlying the two $\delta^+ \to \infty$ limits described above act in concert to attain the overall scale separation, $\delta^+ = \delta/(\nu/u_\tau)$, in turbulent wall flows. These are the mechanisms of spatial confinement (associated with vorticity stretching) and spatial dispersion (associated with advective transport) depicted in figure 3. The present results are concerned with where Ω_z is apportioned as δ^+ increases, and why, as $\delta^+ \to \infty$, the rate at which both Γ_{II}^+ and Γ_{IV}^+ increase is proportional to ϕ_c (Klewicki 2013*a*). In accord with the observations first made by Meinhart & Adrian (1995), figure 3 also depicts how the two self-similar domains described by ϕ relate to an average snapshot of the instantaneous vorticity field. The Reynolds number scaling behaviours of the features are noted on the figure, as is the domain of the L_β layer hierarchy.

In conceptualizing figure 3, and for later reference, it is also useful to recall that vorticity is invariant under Galilean transformation. Thus, relative to the mean, the amplitudes of the vorticity fluctuations in the vortical fissures are large, independent of whether the wall is moving through a stationary fluid or the fluid is moving over a stationary wall. (This is not the case for the velocity fluctuations.) Note further that the enstrophy equation,

$$\tilde{\boldsymbol{\omega}} \cdot \frac{\partial \tilde{\boldsymbol{\omega}}}{\partial t} = -\tilde{\boldsymbol{\omega}} \cdot \nabla \times (\tilde{\boldsymbol{\omega}} \times \tilde{\boldsymbol{V}}) + \nu \tilde{\boldsymbol{\omega}} \cdot \nabla^2 \tilde{\boldsymbol{\omega}}, \tag{1.4}$$

indicates that there are only three mechanisms that can affect a time rate of change at a point. These relate to vorticity advection, vorticity stretching/reorientation (hereafter just called stretching) and viscous diffusion. Furthermore, because pressure does not explicitly appear in the vorticity transport equation, the stretching mechanism is the only one that can cause inter-component exchanges between $\tilde{\omega}_x$, $\tilde{\omega}_y$ and $\tilde{\omega}_z$, or relative to the Reynolds decomposition, exchanges between the mean and fluctuating

Study	Flow configuration	Reynolds number, δ^+
Elsnab *et al.* (2011)	Channel expt	53, 58, 71, 82, 88, 98
Monty (2005)	Channel expt	1453, 1723, 2427, 3118, 3941
Laadhari (2002)	Channel DNS	72, 90, 120
Abe *et al.* (2004)	Channel DNS	640, 1020
Hoyas & Jimenez (2006)	Channel DNS	186, 547, 934, 2004
McKeon (2003)	Pipe expt	$1800 \lesssim \delta^+ \lesssim 530\,000$ (18 values)
Cheng (2011)	Pipe DNS	91, 111, 157, 171, 314, 500, 1000
Wu & Moin (2008)	Pipe DNS	1142
Klewicki & Falco (1990)	TBL expt	375, 970, 1500
Nagib, Chauhan & Monkewitz (2007)	TBL expt (NDF)	5406, 12\,007, 18\,758
Nagib *et al.* (2007)	TBL expt (MTL)	5391, 7556, 10\,815
Hutchins *et al.* (2009)	TBL expt	2476, 3433, 6445, 11\,958, 16\,708
Oweis *et al.* (2010)	TBL expt	17\,000, 32\,000, 47\,000
Priyadarshana & Klewicki (2004)	TBL expt (SLTEST)	890\,000
Wu & Moin (2009)	TBL DNS	53, 85, 145, 211, 273, 327, 368, 396
Schlatter & Orlu (2010)	TBL DNS	357, 671, 1034, 1245

TABLE 2. Investigation, flow configuration, and Reynolds numbers of the primary data sets employed herein. Note that NDF and MTL denote data originating from the National Diagnostic Facility and Minimum Turbulence Level wind tunnels, respectively. SLTEST denotes measurements acquired in the atmospheric surface layer over the salt playa of Utah's western desert. All δ^+ values for the boundary layer data use δ_{99}.

enstrophy. Herein we demonstrate that in the domain where $\phi = \phi_c$ (i.e. the log layer) $\langle \tilde{\omega}^2 \rangle \to \langle \omega^2 \rangle$ as $\delta^+ \to \infty$. This naturally leads one to surmise that the properties of the mean vorticity and its integral, U, increasingly stem from the much larger vorticity amplitudes internal to the fissures depicted in figure 3. Lastly, note that the velocity–vorticity products in (1.2) appear in the first term on the right of (1.4), which contains the stretching and advection terms.

In what follows, we first examine the mean vorticity properties within the context of figure 3 and the mean dynamical structure described in § 1.2, followed by those associated with the vorticity fluctuations. References to figure 3 are made throughout.

2. Data sets

The stated aims are advanced by exploring vorticity properties using a number of data sets. The data come from both physical and numerical experiments. Table 2 lists most of the data sets used herein, and for each study indicates their Reynolds numbers.

3. Results

This section provides evidence supporting the vorticity field depiction of figure 3. Evidence from only one of the canonical flows is typically used to exemplify the given result, with the other results given in the supplemental materials (SM) accompanying this paper available online at http://dx.doi.org/10.1017/jfm.2013.565. We conclude with a brief synopsis of how the present vorticity field results connect to the mean dynamical structure.

3.1. *Mean vorticity organization at the onset of the four-layer regime*

The magnitude orderings of the terms in the mean momentum equation (table 1) become well-approximated at the close of the transitional regime. That is where this equation begins to admit the self-similar behaviours described by the coordinate stretching function ϕ. Thus, insights are gained by clarifying integral properties of the mean vorticity distribution through the transitional regime, and how these properties qualitatively change in the four-layer regime.

As described by Lighthill (1963), increases in δ^+ through the transitional regime are at first accompanied by the rapid wallward concentration of Ω_z (Elsnab *et al.* 2011; Klewicki *et al.* 2011). This occurs in concert with the emergence of a low-amplitude and relatively slowly attenuating (with increasing y^+) outer region Ω_z profile. This outward spreading of the low-level Ω_z *tail* underlies the eventual development of a logarithmic mean velocity profile (Elsnab *et al.* 2011; Klewicki *et al.* 2011, 2012).

The displacement thickness, δ^*, provides a useful measure of these flow field developments. Typically, δ^* is found by equating the mass flux integral that extends from the surface to δ in an actual wall flow to the mass flux integral associated with a uniform flow at U_∞ (or U_c) that extends from δ to a position $y = \delta^*$ from the surface. For rectangular geometries this equality leads to the familiar expression,

$$\delta^* = \int_0^\delta \left(1 - \frac{U}{U_e}\right) \, \mathrm{d}y, \tag{3.1}$$

where U_e refers to U_∞ in the boundary layer and U_c in the channel.

A circular geometry renders the pipe flow calculation somewhat more complicated. The definitional expression,

$$\int_0^R U(r) 2\pi r \, \mathrm{d}r = \int_0^{R-\delta^*} U_c 2\pi r \, \mathrm{d}r, \tag{3.2}$$

can, however, be rearranged into the quadratic form,

$$\left(\frac{\delta^*}{\delta}\right)^2 - 2\left(\frac{\delta^*}{\delta}\right) + \frac{I}{\delta^2} = 0, \tag{3.3}$$

where,

$$I = \int_0^\delta \left(1 - \frac{U(r)}{U_c}\right) 2r \, \mathrm{d}r. \tag{3.4}$$

Lighthill (1958) suggested that a more rigorous definition of δ^* involves representing the layer of Ω_z that resides between $0 \leqslant y \leqslant \delta$ with a single vortex sheet of equivalent Γ_e that also satisfies $U = 0$ at $y = 0$. To within an error of order $(\delta/\ell)^2$ (where ℓ is the flow development length), the position of this vortex sheet is given by

$$\delta^* = \frac{\int_0^\delta y\Omega_z \, \mathrm{d}y}{\int_0^\delta \Omega_z \, \mathrm{d}y} = \frac{\int_0^\delta (U_e - U(y)) \, \mathrm{d}y}{U_e}, \tag{3.5}$$

where (3.5) employs the boundary layer approximation, $|\Omega_z| = |\partial U/\partial y| \gg |\partial V/\partial x|$, but is exact in channel flow. It shows that δ^* physically locates the *centroid of the mean vorticity* (Lighthill 1958).
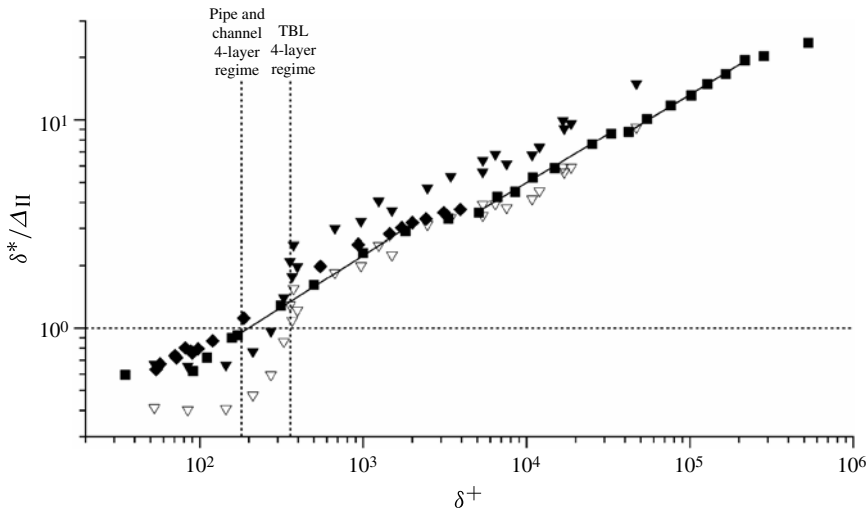
FIGURE 4. Ratio of the displacement thickness to the thickness of layer II versus δ^+: boundary layer data ($\blacktriangledown$); channel flow data ($\blacklozenge$); pipe flow data ($\blacksquare$); boundary layer $\delta^*/(\Delta_{\mathrm{II}} + \Delta_{\mathrm{III}})$ ($\triangledown$)

The evolution of δ^*/δ with increasing δ^+ is presented in the SM, along with an analysis of the contributions from layers I–IV to δ^* for increasing δ^+. Here we focus on the characteristics of δ^* relative to the emergence of the four-layer structure.

The thickness of layer II (table 1) decreases relative to δ like $1/\sqrt{\delta^+}$, while the ratio of the layer II circulation to Γ_e remains $\simeq 1/2$ independent of δ^+. Relative to δ, δ^* rapidly migrates toward the surface with increasing δ^+ in the transitional regime, but once in the four-layer regime this wallward trend slows abruptly. In the four-layer regime the position where $\Gamma = \Gamma_e/2$ is located at the outer edge of layer II (table 1). Thus, $\delta^*/\Delta_{\mathrm{II}}$ is the ratio of the Ω_z profile centroid to the position where its integral is $1/2$ of its total.

Profiles of $\delta^*/\Delta_{\mathrm{II}}$ versus δ^+ for channel, pipe, and boundary layer flow are shown in figure 4. A number of features are evident. Within the laminar and transitional regimes, the centroid of the mean vorticity lies interior to the position where $\Gamma = \Gamma_e/2$, and thus $\delta^*/\Delta_{\mathrm{II}} < 1.0$. With increasing δ^+, this ratio crosses through 1.0. The pipe and channel data first exceed 1.0 at $\delta^+ \simeq 180$. This position closely coincides with the onset of the four-layer regime as determined using a magnitude ordering analysis of the mean momentum equation (Elsnab *et al.* 2011; Klewicki *et al.* 2012). The boundary layer $\delta^*/\Delta_{\mathrm{II}}$ data cross close to but slightly before its similarly estimated start of the four-layer regime (Klewicki *et al.* 2011). It is observed, however, that the ratio $\delta^*/(\Delta_{\mathrm{II}} + \Delta_{\mathrm{III}})$ for the boundary layer data crosses unity almost exactly at the four-layer onset, and shows much closer agreement with the channel and pipe data at higher δ^+. This may have a connection to the absence of a mean surface vorticity flux and outer region mean vorticity annihilation process in the boundary layer, as both exist in the channel and pipe. Regardless, the boundary layer data indicate that both $\delta^*/\Delta_{\mathrm{II}}$ and $\delta^*/(\Delta_{\mathrm{II}} + \Delta_{\mathrm{III}})$ increase rapidly at the close of the transitional regime, and then abruptly change slope at the start of the four-layer regime.

The results of figure 4 show that $\delta^*/\Delta_{\mathrm{II}} > 1$ is the mean vorticity indicator for the beginning of the four-layer regime. The four-layer onset also corresponds to

when the hierarchy length scale distribution, $W^+(y^+)$, first begins to exhibit a short segment of approximately linear dependence on y^+. This linear dependence initiates near $y^+ = 2.6\sqrt{\delta^+}$, and grows like $d\Delta_{IV}^+/d\delta^+ \simeq 1 - 1.3/\sqrt{\delta^+}$ (Klewicki 2013a). It coincides with an emerging logarithmic-like dependence in the mean velocity profile (Fife *et al.* 2009; Klewicki *et al.* 2011; Klewicki 2013a).

The behaviours in figure 4 are associated with the formation of the low-level outer tail of mean vorticity discussed above. Morrill-Winter & Klewicki (2013) surmise that this arises in concert with a scale separation that physically results from motions bearing concentrated vorticity being intermittently dispersed over layer IV. Consistently, figure 3 depicts large-scale zones of increasingly uniform momentum (as $\delta^+ \to \infty$) that are segregated by the vortical fissures. These vortical fissures begin to spatially disperse at the start of the four-layer regime, as reflected by δ^*/Δ_{II} exceeding unity. This process underlies the skewing of the weight in the Ω_z distribution that inherently causes its centroid to reside at an increasingly greater y location than its midpoint.

The four-layer regime pipe flow profile of figure 4 (which covers the largest δ^+ range) exhibits what appears to be a series of *dwells* in slope at about one decade intervals in δ^+. This behaviour is made apparent by the series of power function curve-fits beginning near $\delta^+ = 180$. In accord with the known behaviours of δ^*/δ and Δ_{II}/δ (table 1), each of these curve-fits has a slope of $\sim 1/2$ (0.5 ± 0.02). Examination of the channel and boundary layer profiles in figure 4 reveal that, at a minimum, they also undergo the first dwell. The physical significance of these regular changes in the observed slope is currently unknown.

3.2. *Mean vorticity field scaling and development*

Some elements of the momentum equation analyses concern directly the scaling properties of the mean vorticity distribution, as depicted in figure 3. Testing the results of these analyses with wall-flow data exposes the properties of the mean vorticity distribution relative to the layer boundaries of table 1, and clarifies the self-similar behaviours that underlie the emergence of a logarithmic mean velocity profile.

The analysis of Fife *et al.* yields order-of-magnitude estimates describing the decay rate of dU^+/dy^+ from layer I to layer III (Fife *et al.* 2005b, 2009),

$$y^+ = O(1/\epsilon), \quad |\Omega_z^+| = \frac{dU^+}{dy^+} = O(\epsilon). \tag{3.6}$$

Similarly, by the upper end of the hierarchy, $\eta = y/\delta \simeq 0.5$,

$$|\Omega_z^+| = \frac{dU^+}{dy^+} \geqslant O(\epsilon^2), \quad \frac{dU^+}{d\eta} \geqslant O(1), \tag{3.7}$$

see Wei *et al.* (2005) and Fife *et al.* (2005a). Together, (3.6) and (3.7) prescribe the behaviours sketched in figure 5. $|\Omega_z|$ retains its maximal value of $u_\tau/(v/u_\tau) = u_\tau^2/v$ from the wall out to $y \lesssim 3v/u_\tau$ (outer edge of layer I). It then drops to a value that is $O(u_\tau/\sqrt{v\delta/u_\tau}) = O(\sqrt{u_\tau^3/v\delta})$ by $y = O(\sqrt{v\delta/u_\tau})$, i.e. in or near layer III. From there it subsequently decreases much more slowly to values approaching $O(u_\tau/\delta)$ near the upper end of the hierarchy. Thus, $|\Omega_z|$ is approximately equal to u_τ divided by v/u_τ at the lower boundary of the hierarchy ($y^+ \simeq 7$), and is approximately equal to u_τ divided by δ at the upper end of the hierarchy. The full span of the length scale variation is given by the ratio $\delta/(v/u_\tau) = \delta^+ = \epsilon^{-2}$. This overall scale separation is segregated into two parts: (i) from the wall to the position where $|\Omega_z| = O(\epsilon)$, with the corresponding
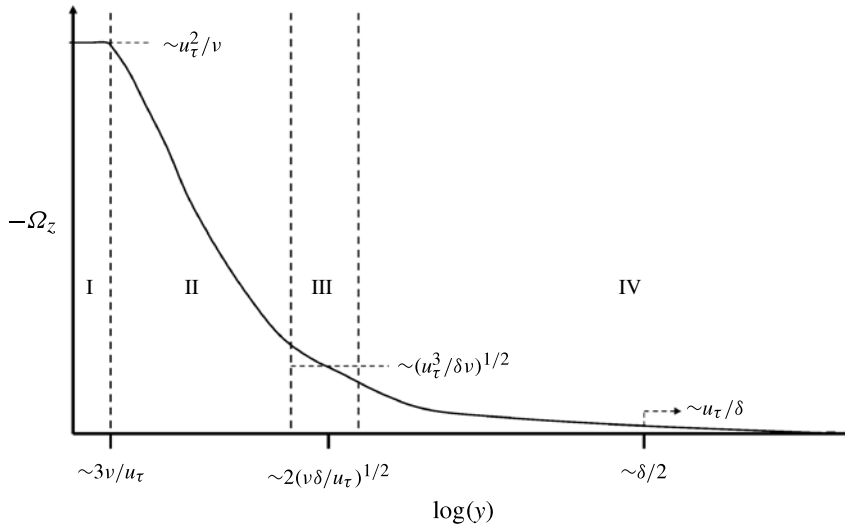
FIGURE 5. Sketch of the mean vorticity profile indicating the rate of decay of $|\Omega_z|$ with distance from the wall as indicated by the theory (Wei *et al.* 2005; Fife *et al.* 2009; Klewicki 2013*a*).

variation in length scale described by the ratio

$$O\left(\frac{\sqrt{\nu\delta/u_\tau}}{\nu/u_\tau}\right) = O(\epsilon^{-1}), \tag{3.8}$$

and (ii) from this position to the upper end of the hierarchy, with the corresponding variation in length scale described by the ratio

$$O\left(\frac{\delta}{\sqrt{\nu\delta/u_\tau}}\right) = O(\epsilon^{-1}). \tag{3.9}$$

Equations (3.8) and (3.9) specify the length scale variations associated with the increments of U^+ in the two regions of the L_β hierarchy depicted in figures 1 and 2, and with the regions of vorticity stretching and dispersion in figure 3. These regions are dynamically distinct; on the former domain the *VF* term in (1.1) is leading order, and on the latter domain it is not.

Data from the studies of table 2 were used to test the veracity of (3.6) and (3.7). Figure 6 presents results for pipe flow, while the boundary layer and channel results are presented in the SM. The decay rate of $|\Omega_z|$ across layer II is explored via the quantity y_ϵ^+, defined as the y^+ position where $|\Omega_z^+|$ equals $\epsilon = 1/\sqrt{\delta^+}$. This quantity is plotted relative to the vertical axis on the left of figure 6. The value of $|\Omega_z|$ at the position of W_{max} (upper end point of the L_β hierarchy, $y/\delta = y_{po}/\delta \simeq 0.5$, see figure 1) is given by the outer-normalized magnitude of the mean vorticity at $\eta = y/\delta = 0.5$, $\mathrm{d}U^+/\mathrm{d}\eta|_{W_{max}}$. Similarly, the net mean circulation (per unit length) in the remainder of the layer ($\eta \geqslant 0.5$) is quantified by $U_c^+ - U_{W_{max}}^+$. Both $\mathrm{d}U^+/\mathrm{d}\eta|_{W_{max}}$ and $U_c^+ - U_{W_{max}}^+$ are referenced to the vertical axis on the right of the figure.

The analysis predicts that y_ϵ^+ should vary like $\xi\sqrt{\delta^+}$, where ξ is an $O(1)$ constant. Accordingly, curve-fits of the y_ϵ^+ data were constrained to adhere to a $\sqrt{\delta^+}$ dependence. Under this constraint, ξ was found to equal 2.48, 2.61 and 2.53 for the channel,
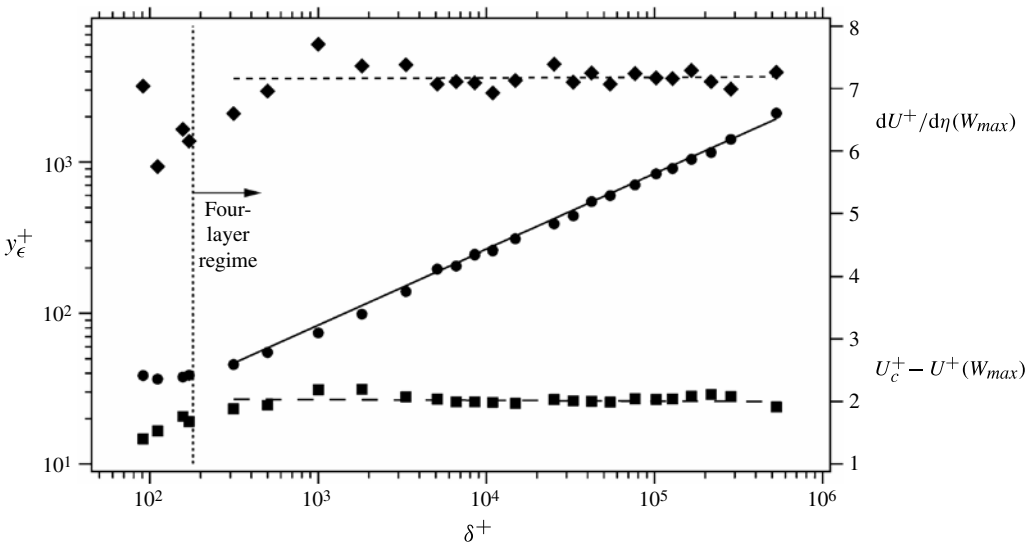
FIGURE 6. Pipe flow mean vorticity profile properties versus δ^+: $y_\epsilon^+ = y^+$ position where $dU/dy = u_\tau/\sqrt{\nu\delta/u_\tau}$ (●); $U_c^+ - U^+(y/\delta = 0.5)$ (■); $dU^+/d\eta(y/\delta = 0.5)$ (♦); $y_\epsilon^+ = 2.61\sqrt{\delta^+}$ (——); $U_c^+ - U^+ = 2.03 - (6.82 \times 10^{-8})y^+$ (– – –); $dU^+/d\eta = 7.15 - (6.38 \times 10^{-8})y^+$ (- - - -). Estimated δ^+ for the onset of the four-layer regime is based upon the study of Klewicki *et al.* (2012).

Flow	ξ	γ	α	$U_e^+ - U_{W_{max}}^+$	$dU^+/d\eta\|_{W_{max}}$
Channel	2.48	1.54	0.563	1.75	6.24
Pipe	2.61	1.51	0.547	2.03	7.15
Boundary layer	2.53	2.11	0.522	2.66	9.86

TABLE 3. Summary of mean circulation and mean vorticity analysis. Fit parameters for $y_\epsilon^+ = \xi\epsilon^{-1} = \xi(\delta^+)^{0.5}$ and $y_\epsilon^+ = \gamma(\delta^+)^\alpha$. Constant terms in the straight line fits to $U_e^+ - U_{W_{max}}^+$ and $dU^+/d\eta\|_{W_{max}}$.

pipe and boundary layer, respectively (table 3). Thus, these findings support the conclusion that y_ϵ^+ is consistently located near the outer edge of layer III. The same data were also fitted according to the more general relation, $y_\epsilon^+ = \gamma y^{+\alpha}$. As summarized in table 3, these curve-fits yield α values between 0.522 and 0.563 with the corresponding γ values ranging between 2.11 and 1.51. From visual comparisons of these curve-fits (not shown), it is not apparent that those for which both γ and α are allowed to vary provide characterizations of the data trends superior to those for which γ is constrained to equal 0.5. In either case, these results are deemed to be well-aligned with the analytical predictions.

For sufficiently high Reynolds numbers, the behaviours of $dU^+/d\eta\|_{W_{max}}$ and $U_c^+ - U_{W_{max}}^+$ exhibit similar agreement with the analytical estimates. From (3.7) it is expected that $dU^+/d\eta\|_{W_{max}}$ will approach an essentially constant value having magnitude not less than $O(1)$. For each of the three flows, a linear curve-fit of

the $dU^+/d\eta|_{W_{max}}$ data has negligible slope, with the constant term ranging from 6.24 to 9.86 (table 3). The $U_c^+ - U_{W_{max}}^+$ data also develop constant values of ~1.75, 2.03, and 2.66 for the channel, pipe, and boundary layer, respectively. The $U_c^+ - U_{W_{max}}^+$ behaviours are similar to those exhibited by the parameter Π in the Coles (1956) wake model. Overall, the $dU^+/d\eta|_{W_{max}}$ and $U_c^+ - U_{W_{max}}^+$ results reveal that the boundary layer contains the largest amount of outer region vorticity (both in an integral sense and at $\eta = 0.5$), followed by the pipe, and then the channel. Other differences between the pipe, channel and boundary layer are discussed in the SM.

Expressions (3.6) and (3.7), as tested above, provide insight into the Ω_z profile development. By the close of the transitional regime, wall-flow dynamics are acting to concentrate about half of the total Ω_z into a near-wall domain that, relative to δ, is shrinking like $\epsilon = 1/\sqrt{\delta^+}$. The remainder of the Ω_z is spread over a layer IV domain of size that is approaching δ at a rate approximated by $1 - 1.3/\sqrt{\delta^+}$ (Klewicki 2013a). Transitional flow studies indicate that this occurs owing to the spread of turbulent inertia from near the initial peak in the T^+ ($= -\langle uv \rangle^+$) profile toward the periphery of the flow (Elsnab *et al.* 2011; Klewicki *et al.* 2011, 2012). Near the close of the transitional regime, the minimum and maximum length scales of the motions associated with *TI* become constrained by the boundary conditions. This marks when ν/u_τ and δ become parameters relevant to scaling the properties of the four-layer regime, as it also marks when the end points of the L_β hierarchy become fixed at $y^+ = y_{pi}^+ \simeq 7$ and $y/\delta = y_{po}/\delta \simeq 0.5$, respectively, see figure 1(b) and Klewicki *et al.* (2011). As implied by the depiction of figure 3, this same process continues in the four-layer regime, since with each increment in δ^+ the layer hierarchy expands to fill the domain between y_{pi} and y_{po}.

These findings collectively indicate that the limiting values of the mean vorticity profile can be made the same at any given δ^+ by multiplying Ω_z^+ by $\epsilon^{-1} = \sqrt{\delta^+}$, and multiplying y^+ by ϵ. When these quantities are plotted on linear axes, the profile rapidly becomes characterized by two 'δ-functions' (spikes) of magnitude ϵ^{-1} that, with increasing δ^+, increasingly become more adjacent to the plot axes. For example, for $\delta^+ \gtrsim 10\,000$ these inner and outer spikes characterizing the profile become indistinguishable from the vertical and horizontal axes, respectively. The transition between the two spikes begins near the outer edge of layer II, and is completed near the outer edge of layer III ($\epsilon y^+ \simeq 2.6$), which also corresponds to y_ϵ^+ (table 3). The region interior to the transition is where vorticity stretching is indicated to be most important in figure 3, while the region beyond the transition is characterized by advective transport. These regions also correspond to layers II and IV, respectively, see table 1.

Boundary layer profiles of $|\Omega_z^+|\epsilon^{-1}$ versus ϵy^+ are shown in figure 7, while those for the channel and pipe are given in the SM. Here it is useful to note that under inner normalization the $|\Omega_z|$ profiles from all of the canonical wall flows are observed to be invariant for $y^+ \lesssim 40$, see the SM. This observation allows the profiles of figure 7 to be extended to the wall using the DNS profile for $y^+ \lesssim 40$. The data of figure 7 support the analytical predictions, and agree with the empirical observations from channels and pipes reported in the SM.

For each of the canonical flows, the $|\Omega_z^+|\epsilon^{-1}$ profiles convincingly merge beginning near $\epsilon y^+ = 2.6$, and for greater ϵy^+ adhere to a power law consistent with a logarithmic mean velocity profile. Recent high-Reynolds-number pipe and boundary layer data provide compelling support for the logarithmic layer beginning near $\epsilon y^+ = 2.6$ (Marusic *et al.* 2013). Aligning the profiles about y_ϵ^+ at each δ^+ has
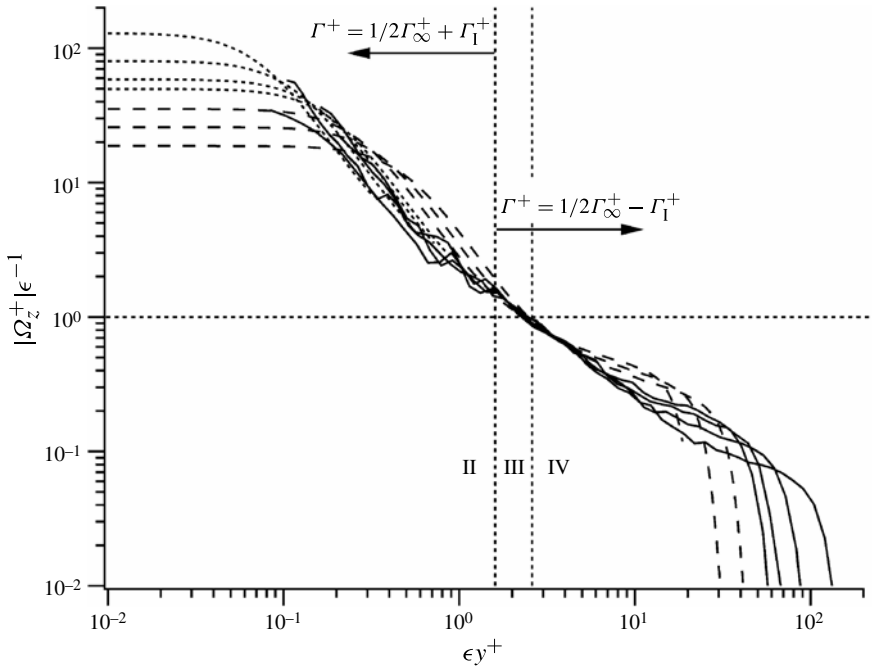
FIGURE 7. Mean vorticity profiles in turbulent boundary layer flow, meso-normalized and plotted on logarithmic axes. Solid lines are from the experiments of Hutchins *et al.* (2009). Dashed lines are from the $\delta^+ = 671$, 1034, and 1245 simulations of Schlatter & Orlu (2010). Dotted lines are DNS profiles that have been transformed to correspond to the δ^+ of the experimental profiles.

significance in describing the development of the mean momentum profile, since, regardless of δ^+, the normalized position where the *VF* term loses leading order remains fixed. That is, while both the present and classical (overlap layer based) formulations include the existence of an asymptotically logarithmic U^+ versus y^+ profile, the classical formulation prescribes an $O(\nu/u_\tau)$ wall-normal extent for the region where viscous effects are leading order, e.g. Yajnik (1970), Mellor (1972) and Wosnik, Castillo & George (2000). A preponderance of evidence, however, indicates that the *VF* term retains leading order to $y = O(\sqrt{\nu\delta/u_\tau})$, and more specifically to $\epsilon y^+ \simeq 2.6$ (Wei *et al.* 2005; Fife *et al.* 2005*a*, 2009; Klewicki 2010).

The above scaling behaviours are more comprehensively understood by recognizing that $W^+(y^+)$ is the natural length scale of the *TI* term in (1.1) (Fife *et al.* 2005*a*, 2009). For this reason, the emerging constancy of $\mathrm{d}W^+/\mathrm{d}y^+ = \phi_c^{-1}$ beyond $\epsilon y^+ \simeq 2.6$ is accurately characterized as the origin of the distance from the wall scaling. This attribute of turbulent wall flows is clarified in figure 8(*a,b*), where $|\Omega_z^+|$ is made dimensionless using $W(y^+)$ and u_τ. (Note that $W^+|\Omega_z^+| = W|\Omega_z|/u_\tau$.)

Figure 8(*a*) shows channel data over the range $186 \leqslant \delta^+ \leqslant 2004$. Under this normalization, the three higher-δ^+ profiles fall on a single curve interior to $y^+ \simeq 40$, while the profile at the very onset of the four-layer regime ($\delta^+ = 186$) deviates slightly. Beyond $y^+ \simeq 40$, each profile reaches a plateau, and the width of this plateau broadens and flattens with increasing δ^+. The vertical dotted lines on this figure denote $\epsilon y^+ = 2.6$ at each δ^+. Each profile consistently breaks away from the $\delta^+ = 2004$ profile near $\epsilon y^+ = 2.6$, while the $\delta^+ = 2004$ profile begins its plateau at this location.
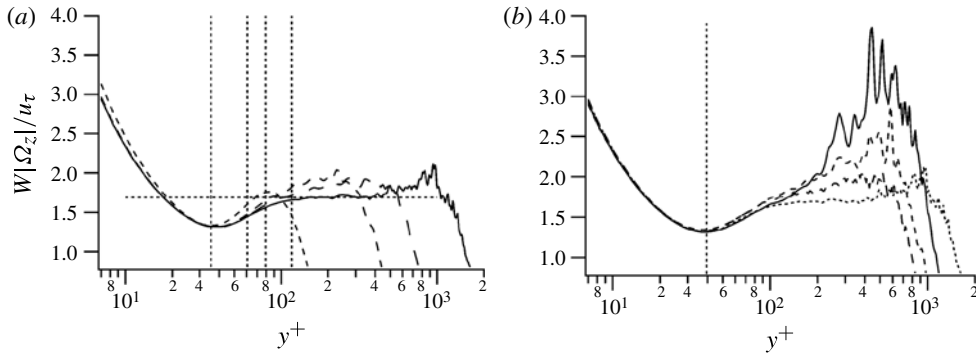
FIGURE 8. Mean spanwise vorticity profiles normalized by u_τ and $W(y^+)$ and plotted versus y^+. (*a*) Channel flow DNS of Hoyas & Jimenez (2006): $\delta^+ = 186$ (- - -); $\delta^+ = 547$ (– – –); $\delta^+ = 934$ (— — —); and $\delta^+ = 2004$ (——). Vertical dotted lines denote outer edge of layer III for each respective flow. Horizontal dotted line denotes a curve-fit of the $\delta^+ = 2004$ data and is equal to 1.72. (*b*) Pipe flow DNS of Wu & Moin (2008) at $\delta^+ = 1142$ (- - -); boundary layer DNS of Schlatter & Orlu (2010) at $\delta^+ = 1245$ (——); channel flow DNS of Abe *et al.* (2004) at $\delta^+ = 1020$ (– – –); channel flow DNS of Hoyas & Jimenez (2006) at $\delta^+ = 2004$ (· · · · ·).

At $\delta^+ = 186$ the outer edge of layer III lies interior to $y^+ = 40$, i.e. there is negligible spatial separation between the near-wall processes that occur in the region $y^+ \lesssim 40$ and the inertial mean dynamics of layer IV. Thus, the plateau region at $\delta^+ = 186$ is non-existent.

The development of the profiles in figure 8(*a*) with increasing δ^+ is anticipated from analysis of the mean momentum equation (Fife *et al.* 2009). The emergence of the increasingly well-defined plateau reflects the increasingly self-similar mean dynamics on the $\phi = \phi_c$ portion of the L_β hierarchy. This is the region where advective transport becomes largest in figure 3. The analysis that results in the logarithmic mean profile equation,

$$U^+ = \phi_c^2 \ln(y^+ - C) + D, \tag{3.10}$$

stems from

$$\frac{\mathrm{d}U^+}{\mathrm{d}y^+} = \frac{\phi_c^2}{(y^+ - C)}, \tag{3.11}$$

where the constant, C, is the predicted offset (Fife *et al.* 2009; Klewicki 2013*a*). Accordingly, $W^+(y^+)$ is increasingly well-approximated by the linear function,

$$W^+(y^+) = \frac{y^+}{\phi_c} + B, \tag{3.12}$$

on this portion of the hierarchy. Analysis of the $\delta^+ = 2004$ channel flow yields the estimates $\phi_c \simeq 1.6$ and $B \simeq 5.6$ (Klewicki *et al.* 2009). Owing to (3.12), (3.11) can be written as

$$(W^+ - B)\frac{\mathrm{d}U^+}{\mathrm{d}y^+} = \frac{y^+ \phi_c}{(y^+ - C)} \tag{3.13}$$

on this portion of the hierarchy. Equation (3.13) shows that the effects of the constants B and C diminish as $\delta^+ \to \infty$, i.e.

$$W|\Omega_z|/u_\tau \to \text{constant} = \phi_c. \qquad (3.14)$$

The horizontal line fit to the $\delta^+ = 2004$ profile in figure 8(a) has a value of 1.72, whereas a fit that includes the constant, B, levels off at 1.66. Use of these values and $\phi_c \simeq 1.6$ in (3.13) yields an estimate for the offset of $C \simeq 9$, which nominally agrees with the theoretical prediction of ~ 7 and the value of 8 empirically estimated by Wosnik *et al.* (2000). The use of $W(y^+)$ and u_τ to normalize the mean vorticity is similar to the so-called indicator function, $\Xi = y^+ \mathrm{d}U^+/\mathrm{d}y^+$, that is often used to detect the existence of logarithmic dependence, and in fact the two measures become exactly proportional as $\delta^+ \to \infty$. Normalization using W and u_τ is, however, related to the emergence of the $\phi = \phi_c$ self-similarity, as admitted by the mean momentum equation.

Figure 8(b) shows $\delta^+ \simeq 1000$ profiles of $W|\Omega_z|/u_\tau$ versus y^+ from channel, pipe, and boundary layer flows. For comparison, this figure also shows the channel profile at $\delta^+ = 2004$. For $y^+ \lesssim 40$ all of the data follow the same profile. At $y^+ \simeq 40$ these profiles attain their minimum value, after which they begin to exhibit small but discernible differences out to the outer edge of layer III ($83 \lesssim y^+ \lesssim 92$, depending on the flow). These slight deviations are consistent with $|\Omega_z^+|$ versus y^+ exhibiting a weak Reynolds number dependence in the region $40 \lesssim y^+ \lesssim 2.6\sqrt{\delta^+}$ (Klewicki 2013a). Into layer IV, the profiles exhibit dramatic differences. From these data it is clear that the pipe and boundary layer develop a constant plateau more slowly than in the channel. This correlates with these flows having a higher accumulation of mean vorticity in the outer part of layer IV. The boundary layer profile exhibits the greatest outer region peak, while the pipe profile proportionally exhibits the most weight closest to $y/\delta = 1$.

3.3. *Fluctuating vorticity field development and scaling*

Analyses employing the methods of Fife *et al.* (2005b) have yet to be conducted on the equations that describe the vorticity variances. The discussion of (1.4) leads one to suspect, however, that the mean and fluctuating fields will develop self-similarly. Beyond $\epsilon y^+ \simeq 2.6$, advective transport via $\langle v\omega_z \rangle$ is the largest contributor to the *TI* term in (1.1), see figure 2. Furthermore, the dominance of the vorticity fluctuation amplitudes relative to the mean on this domain is verified in figure 10 below. These features are consistently depicted in figure 3, where the layer IV structure is characterized by narrow fissures of elevated vorticity immersed within a much lower-vorticity background flow. We now explore whether the distributions of the mean and fluctuating vorticity exhibit self-similarity with distance from the wall and Reynolds number (as implied by the depiction of figure 3), and clarify how the velocity–vorticity correlations in (1.2) contribute to the distribution of the *TI* term given in figure 1(b).

The results of §3.2 naturally lead to consideration of ω_z' normalized by $W(y^+)$ and u_τ. Figure 9(a,b) shows these profiles for channel and boundary layer flows, respectively. Both plots reveal that these profiles rapidly approximate an invariant function of y^+ out to near layer III. From there they provide evidence of an emerging self-similar structure at greater y^+ for increasing δ^+. For reference, in the channel $y^+ \simeq 2.6\sqrt{\delta^+}$ moves from $y^+ \simeq 36$ at $\delta^+ = 186$ to $y^+ \simeq 116$ at $\delta^+ = 2004$. Over the domain where $\phi = \phi_c$, the $\delta^+ = 2004$ profile of figure 9(a) convincingly develops a region of constant slope, with the equation for the curve-fit indicated on the graph. This curve-fit was made over the domain $115 \lesssim y^+ \lesssim 500$, which coincides with that used by Klewicki *et al.* (2009) to estimate the value of ϕ_c for this flow. (Plotting these data on a semi-logarithmic axes, not shown, also reveals evidence of a constant slope
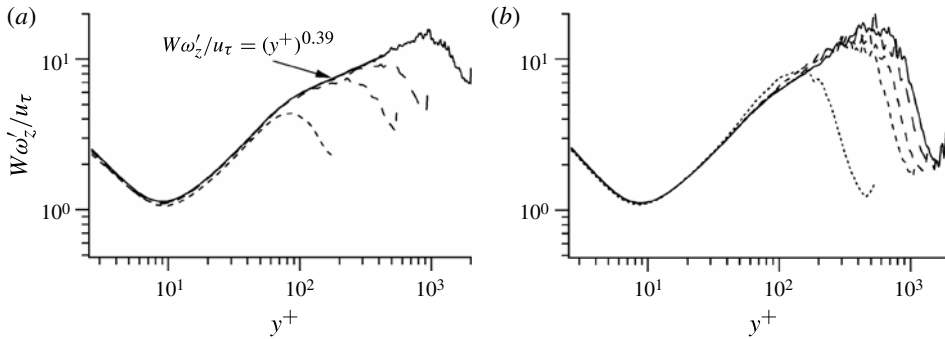
FIGURE 9. Spanwise vorticity intensity profiles normalized by u_τ and $W(y^+)$ and plotted versus y^+. (*a*) Channel flow DNS of Hoyas & Jimenez (2006): $\delta^+ = 186$ (- - -); $\delta^+ = 547$ (– – –); $\delta^+ = 934$ (— — —); and $\delta^+ = 2004$ (——). (*b*) Boundary layer DNS of Schlatter & Orlu (2010): $\delta^+ = 359$ (· · ·); $\delta^+ = 830$ (- - -); $\delta^+ = 974$ (– – –); $\delta^+ = 1145$ (— — —); and $\delta^+ = 1271$ (——).
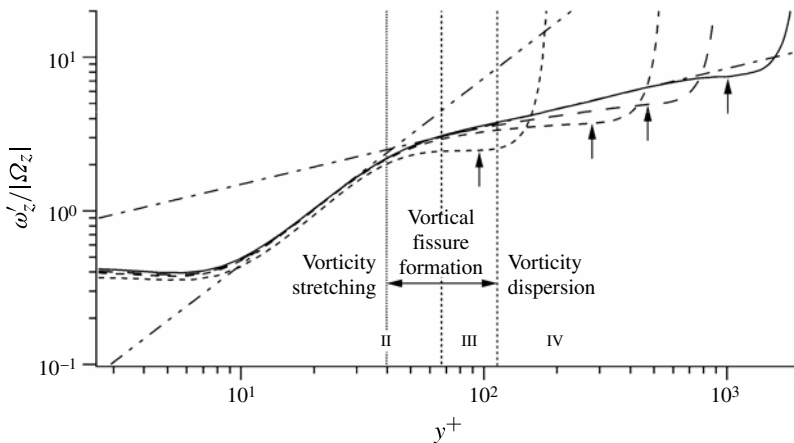

FIGURE 10. Spanwise vorticity intensity profiles from the channel flow DNS of Hoyas & Jimenez (2006), normalized by $|\Omega_z|$ and plotted versus y^+. Profile line styles are the same as in figure 9(*a*). The vertical dotted line indicates $y^+ = 40$. The vertical dashed lines indicate the inner and outer boundaries of layer III at $\delta^+ = 2004$. Arrows indicate the position of W_{max} in each of the profiles. Curve-fit in layer II is given by $\omega_z'/|\Omega_z| = 0.027(y^+)^{1.21}$. Curve-fit in layer IV is given by $\omega_z'/|\Omega_z| = 0.626(y^+)^{0.38}$.

in the domain where $\phi = \phi_c$.) For greater y^+, the data are somewhat more scattered, but essentially follow the same trend out to the upper limit of the L_β hierarchy, i.e. a curve-fit out to $y^+ \simeq 1000$ yields a slope of 0.41. Higher-Reynolds-number data are needed ascertain if this region of constant slope persistently extends to the top of the hierarchy ($y/\delta \simeq 0.5$). The boundary layer profiles of figure 9(*b*) exhibit a similarly emerging constant slope region, but also reinforce that the channel approaches the high-δ^+ self-similar state more quickly that the pipe, and especially the boundary layer.

Figures 8 and 9 provide evidence that, with increasing δ^+, both the Ω_z and ω_z' profiles increasingly scale when made dimensionless using u_τ and $W(y^+)$. Thus, they

also develop similarly relative to each other, as demonstrated in figure 10. Interior to the start of the L_β hierarchy ($y^+ = y_{pi}^+ \simeq 7$), the $\omega_z'/|\Omega_z|$ profile is nearly constant $\simeq 0.4$. Close examination reveals a weak δ^+ dependence that is consistent with that exhibited by the wall value of $\omega_z'^+$ (Klewicki 2010). This near-constancy also reflects the fact that the ω_z fluctuations and the instantaneous total spanwise vorticity, $\tilde{\omega}_z$, are highly correlated owing to the no-slip wall. Beyond $y^+ = y_{pi}^+ \simeq 7$, all of the profiles in figure 10 rapidly rise, and over the domain $13 \lesssim y^+ \lesssim 37$ exhibit a nearly constant slope of ~ 1.21. Once again, the $\delta^+ = 186$ profile deviates slightly from the others.

For $y^+ \gtrsim 40$ (vertical dotted line), the profiles in figure 10 begin to transition to a different slope. This transition culminates near $\epsilon y^+ = 2.6$, beyond which the slope regains approximate constancy. The y^+ extent of this layer IV constant slope region increases with increasing δ^+, and coincides with the region of $\phi = \phi_c$ similarity. This is most apparent in the $\delta^+ = 2004$ profile. The persistence of this constant slope region requires verification at higher δ^+. The curve-fit on the graph was determined over the same domain as the curve-fit in figure 9(*a*). It has a slope of 0.38. For $\delta^+ = 2004$, ω_z' exceeds $|\Omega_z|$ by a factor of ~ 3.75 (or $\langle \omega_z^2 \rangle / \langle \Omega_z^2 \rangle \gtrsim 14$) at $y^+ = 2.6\sqrt{\delta^+}$. Thus, on the domain of advective transport in figure 3 the fluctuations about the mean are increasingly indicative of $\tilde{\omega}_z$.

All of the profiles in figure 10 exhibit a region of constant plateau prior to the upper end of the hierarchy. The location of W_{max} is indicated on each profile by the arrow. The position where the $\delta^+ = 2004$ profile breaks from its upward constant slope correlates with where the mean profile similarity solution begins to detectably deviate from the DNS solution (Klewicki 2013*a*). It also corresponds closely with the position where the $\langle w\omega_y \rangle$ correlation changes sign in figures 2 and 13. The boundary layer profiles shown in the SM exhibit similar properties as described for the channel, but like in figure 8 are less well-developed.

Features of figure 10 are relevant to figure 3. The near-wall region of constant slope in figure 10 is predominantly associated with the physical mechanism of vorticity stretching, which accounts for an exchange from Ω_z to ω_z, and the inter-component exchanges between ω_z, ω_x, and ω_y. The vortical motions resulting from this mechanism continue to stretch in the region $40 \lesssim y^+ \lesssim 2.6\sqrt{\delta^+}$ as they organize into the vortical fissures first observed by Meinhart & Adrian (1995). In this region, the mean viscous force (*VF*) term in (1.1) retains leading order, and the inertial contributions are characterized by a decreasing influence of vorticity stretching. Figure 10 indicates that the layer IV vorticity field is dominated by the fluctuations and increasingly so as $\delta^+ \to \infty$. The layer IV region of constant slope coincides with a mean momentum balance whose dominant terms are inertial, and this slope is predominantly associated with the advective spatial dispersion of the vortical fissures. This mechanism of transport adheres to the distance from the wall scaling dictated by the linear $W^+(y^+)$ distribution ($\phi = \phi_c$ coordinate stretching). Statistical descriptions based upon the attached-eddy model are consistent with this mechanism (Townsend 1976; Perry & Chong 1982; Perry, Henbest & Chong 1986; Perry & Marusic 1995).

The above description is supported by the greater importance of $\langle w\omega_y \rangle$ in layer II and similarly for $\langle v\omega_z \rangle$ in layer IV, as these correlations are associated with vorticity stretching and advection, respectively, e.g. Tennekes & Lumley (1972). It is easily reasoned that vorticity stretching is the dominant mechanism underlying the three-dimensionalization of the near-wall vorticity field. Consistently, analysis of the mean enstrophy equation in the SM reveals that for $y^+ \lesssim 40$ vorticity stretching underlies an exchange of enstrophy from the mean to the fluctuations that coincides with the rapid
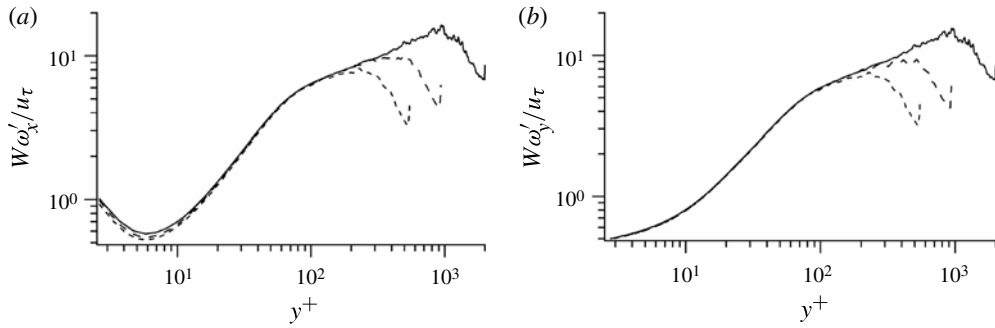
FIGURE 11. Streamwise (*a*), and wall-normal (*b*), vorticity intensity profiles from the channel flow DNS of Hoyas & Jimenez (2006), normalized by u_τ and $W(y^+)$ and plotted versus y^+: $\delta^+ = 547$ (- - -); $\delta^+ = 934$ (– – –); $\delta^+ = 2004$ (——).
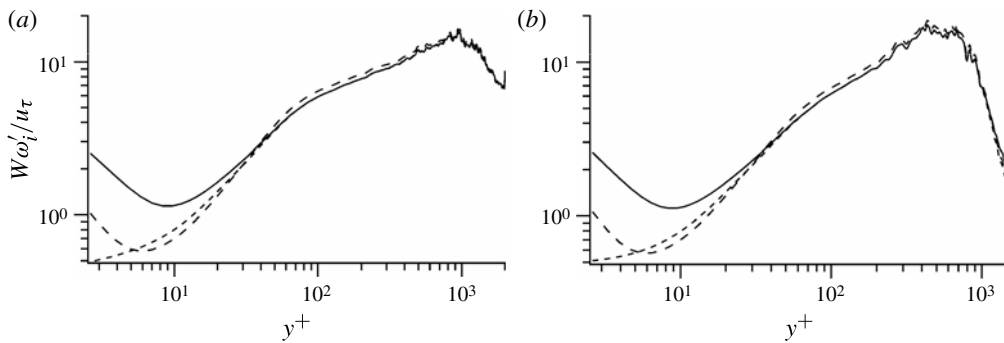

FIGURE 12. Vorticity intensity profiles as normalized by u_τ and $W(y^+)$ and plotted versus y^+, (*a*) from the $\delta^+ = 2004$ channel flow DNS of Hoyas & Jimenez (2006), (*b*) from the $\delta^+ = 1271$ boundary layer DNS of Schlatter & Orlu (2010): $W\omega_x'/u_\tau$ (– – –); $W\omega_y'/u_\tau$ (- - -); $W\omega_z'/u_\tau$ (——).

rise of $\omega_z'/|\Omega_z|$ in figure 10, and the invariant development and equalization of the ω_i' ($i = x, y, z$) shown in figures 11 and 12. Between $y^+ \simeq 40$ and $y^+ \simeq 2.6\sqrt{\delta^+}$, advection becomes more significant, and by the end of layer III, ω_x' and ω_y' develop self-similarly with ω_z' (figure 12). Consonant with self-similar mean dynamics in the domain where $\phi = \phi_c$, the intensities of the two components contributing to (1.2) (ω_y' and ω_z') are indistinguishable. A more detailed discussion of the profiles in figures 11 and 12 is given in the SM.

The contributions from the motions bearing ω_y and ω_z to the mean dynamics are clarified in figure 13, which presents profiles of $W^+\langle v\omega_z\rangle^+$, $W^+\langle w\omega_y\rangle^+$, and their difference, $W^+ dT^+/dy^+$. When the dT^+/dy^+ profile is weighted by W^+ the momentum source and sink portions of the resulting profile on the hierarchy become nearly identical in shape and amplitude (figure 1). In the region where turbulent inertia is a net momentum source, the $W^+\langle w\omega_y\rangle^+$ profile is solely negative, and is the largest contributor to dT^+/dy^+. On the other hand, $W^+\langle v\omega_z\rangle^+$ is positive interior to $y^+ \simeq 8$. Klewicki, Murray & Falco (1994) attribute this to the lifting of sublayer (layer I) streaks, which constitute positive ω_z perturbations. They further surmised
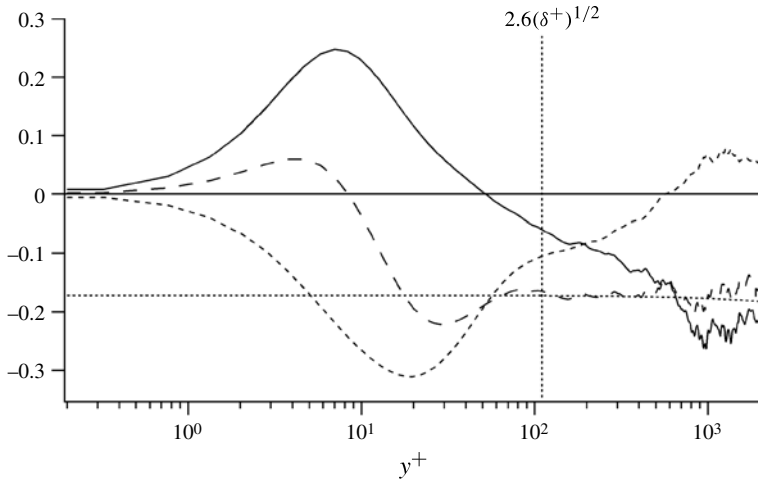
FIGURE 13. Channel flow profiles of the terms in (1.2) weighted by $W^+(y^+)$: $W^+ dT^+/dy^+$ (——); $W^+\langle v\omega_z\rangle^+$ (– – –); $W^+\langle w\omega_y\rangle^+$ (- - -). Data are from the DNS of Hoyas & Jimenez (2006).

that, since the $\tilde{\omega}_z$ in a lifting streak is large and negative, as it moves to increasing y^+ it will quickly become a negative perturbation. At the near-wall zero-crossing of $\langle v\omega_z\rangle^+$, $\langle w\omega_y\rangle^+$ wholly accounts for dT^+/dy^+. Here dT^+/dy^+ is near its maximum, but is decreasing, i.e. is on the hierarchy, $y^+ > y_{pi}^+$. From this position out to y_m^+ (zero-crossing of dT^+/dy^+, figure 1), $W^+\langle w\omega_y\rangle^+$ has greater magnitude than $W^+\langle v\omega_z\rangle^+$, and their diminishing difference accounts for the decrease in dT^+/dy^+. Physically, the intensity of vorticity stretching is decreasing, while the influence of advective transport is increasing. When combined with the results of figures 9–12, these findings support the assertion that vorticity stretching, reorientation and inter-component exchange are most significant on the domain where $\phi \neq$ constant (figure 1).

A relatively simpler structure emerges across layer III and into layer IV, and this is clarified by the W^+ weighting of figure 13. For $y^+ > y_m^+$, the $W^+\langle v\omega_z\rangle^+$ profile levels off, and attains convincing constancy from $\epsilon y^+ \simeq 2.6$ to at least where the $W^+\langle w\omega_y\rangle^+$ crosses zero ($y^+ \simeq 600$). In accord with figure 3, this is clear evidence that the nearly constant and increasingly dominant $W^+\langle v\omega_z\rangle^+$ contribution to the momentum sink-like motions on the domain where $\phi = \phi_c$ results from the decreasing magnitude of $\langle v\omega_z\rangle^+$ being nearly perfectly balanced by the linear increase in $W^+(y^+)$. This further suggests that the distance from the wall scaling (which follows from the asymptotic linearity of W^+) physically derives from concentrated regions of $\tilde{\omega}_z$ (or nearly equivalently, ω_z) being dispersed throughout layer IV at an average rate described by $W^+(y^+)$ (figure 3). Between its near-wall peak and $\epsilon y^+ \simeq 2.6$, the $W^+\langle w\omega_y\rangle^+$ profile exhibits a rapid decrease in amplitude, indicating the attenuation of vorticity stretching. At the start of the region where $\phi = \phi_c$ the $W^+\langle v\omega_z\rangle^+$ contribution is nearly double that of $W^+\langle w\omega_y\rangle^+$. Beyond $\epsilon y^+ \simeq 2.6$ the $W^+\langle w\omega_y\rangle^+$ profile is non-zero, but exhibits an approximately logarithmic decay out to its zero-crossing. Physically, as the vortical fissures disperse, vorticity stretching attenuates (figure 3).

3.4. *Spanwise vorticity length and time scales*

The characteristics of the vortical fissures are now considered. The results of the analysis are consistent with the scaling behaviours of the fissure widths and spacings
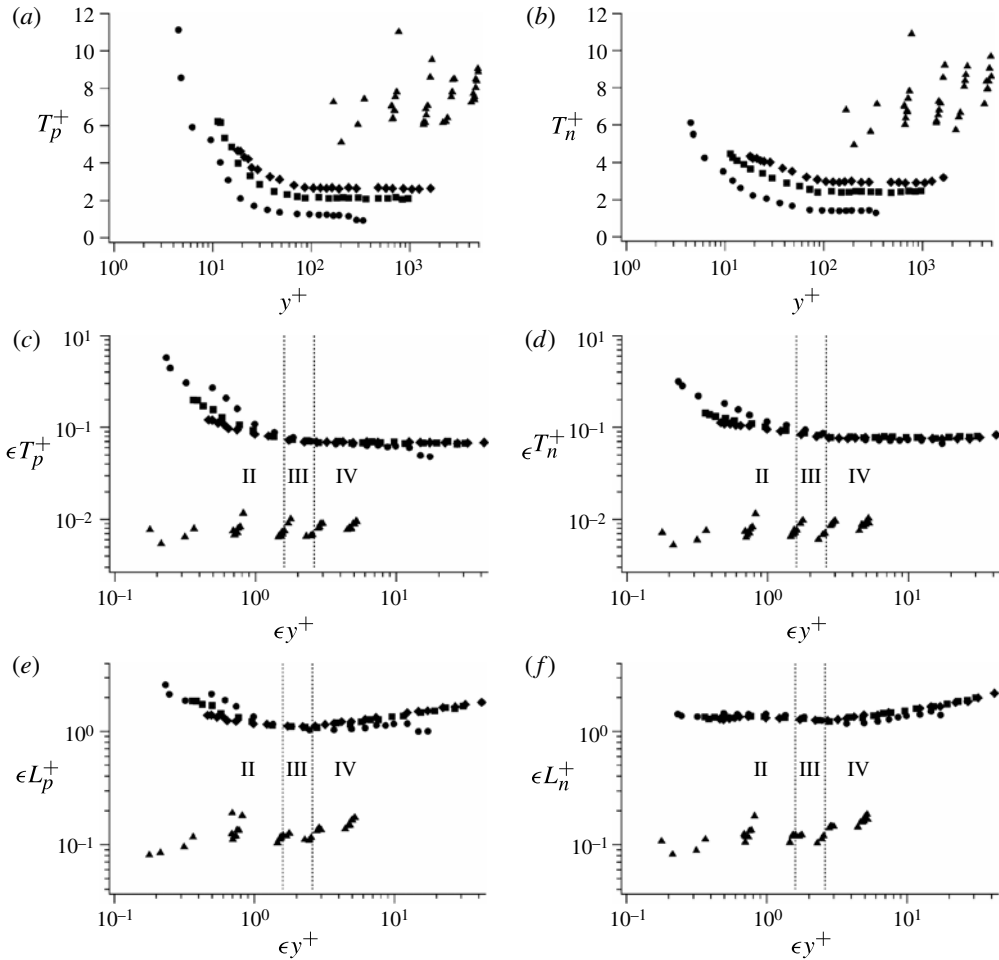
FIGURE 14. Durations and streamwise (advected) lengths associated with ω_z events exceeding $\pm 1.0\omega_z'$: (*a*) inner-normalized positive durations versus y^+, (*b*) inner-normalized negative durations versus y^+, (*c*) meso-normalized positive durations versus ϵy^+, (*d*) meso-normalized negative durations versus ϵy^+, (*e*) meso-normalized positive lengths versus ϵy^+, (*f*) meso-normalized negative lengths versus ϵy^+. $\delta^+ = 375$ (●); $\delta^+ = 970$ (■); $\delta^+ = 1500$ (♦); $\delta^+ \simeq 890\,000$ (▲). Results are derived from the measurements of Klewicki & Falco (1996) and Priyadarshana & Klewicki (2004).

given in figure 3. They are also consistent with the transition from the spatial confinement to advective dispersion mechanism of scale separation across layer III, as also depicted in figure 3.

Time series analyses were used to quantify the duration of positive and negative ω_z events, T_p and T_n respectively, that exceed a given threshold. To account for intermittent signal amplitude deviations from the predominant trend, events were sustained for a 20 % drop below the peak event value, even when the signal amplitude became smaller than the threshold defining the beginning of the event. For the laboratory data sets presented in figure 14, previous analyses indicate that for a range of thresholds equal to or exceeding $1.0\omega_z'$ the event durations are only weakly

dependent on threshold (Klewicki & Falco 1996). Similar dependence is observed for variations in the percentage drop limit. Variations in these parameters cause small proportional variations in the results, and thus Reynolds number dependence is essentially independent of the threshold and percentage drop limit. Event durations were converted to streamwise lengths using the mean velocity, e.g. $L_p = UT_p$.

Figures 14(*a*) and 14(*b*) respectively show profiles of the inner-normalized durations of positive and negative ω_z events at $\delta^+ = 375$, 970, 1500 and approximately 890 000. These exhibit clear variations with δ^+. At any given δ^+, each profile is characterized by relatively large values near the wall that decrease to an outer portion that retains almost exactly constant values. Consistent with the outward motion of layer I streaks, the positive event durations become noticeably larger than the negative ones as the wall is approached. The profiles of figure 14(*a,b*) consistently shift upward with increasing δ^+, and the *knee* that exists between the downward near-wall trend and outer plateau (seen in each of the laboratory profiles) shifts outward with δ^+. Although scattered, the $\delta^+ \simeq 890\,000$ data clearly exhibit larger values.

Figure 14(*c,d*) presents the ω_z event durations under a normalization using $\sqrt{\nu\delta/u_\tau}$ and u_τ. This is a useful surrogate for $W(y^+)$, since it is the width of layer III, the central layer on the hierarchy (Klewicki 2013*a*). The event profiles of figure 14(*c,d*) indicate a rapid shortening of the event durations in layer II, followed by a milder decrease across layer III. Once into layer IV the event durations are remarkably constant; both the $\delta^+ = 970$ and 1500 curves have essentially identical values and individually vary by only $\sim$2.5% peak-to-peak for $\epsilon y^+ > 2.6$. Apparently, the increasing size of the motions corresponding to $\omega_z > 1.0\omega_z'$ is nearly exactly counter-balanced by their increasing advection velocity with increasing y. The $\delta^+ \simeq 890\,000$ data of figure 14(*c,d*) are nominally parallel to but about one decade (in ϵT^+) below the laboratory data.

Figure 14(*e,f*) shows the advected lengths. The laboratory profiles reveal that both the positive and negative event lengths are minimal at $\epsilon y^+ \simeq 2.6$, while the $\delta^+ \simeq 890\,000$ data suggest a shallow minimum in layer III. As in figure 14(*c,d*), these data are about one decade in ϵL^+ below the low-δ^+ profiles. At high Reynolds number the position at which U^+ equals a fixed fraction of U_∞^+ (or U_c^+) moves to increasing y^+ with increasing δ^+ (Metzger & Klewicki 2001). This phenomenon is accounted for by the present framework, as revealed by the scaling behaviour, $\Gamma_{\mathrm{II}} \simeq 0.5\Gamma_\infty$, independent of δ^+. This position resides at $\epsilon y^+ \simeq 1.6$ for all δ^+ (table 1). The results of figure 14(*e,f*) provide evidence that, when combined with the event durations of figure 14(*c,d*), this scaling property causes the minimum streamwise advected length of the ω_z motions to reside near $\epsilon y^+ \simeq 2.6$.

The detailed behaviours of figure 14(*e,f*) are clarified in figure 15, which shows the L_p and L_n data at $\delta^+ = 970$ and $\delta^+ = 1500$ and their average, $(L_p + L_n)/2$, on expanded logarithmic axes. The L_p exceed the L_n near the wall (figure 15*a*). With increasing y, the L_p exhibit a rapid decrease out to near $y^+ = 40$, and continue to decrease, only more slowly, to $\epsilon y^+ \simeq 2.6$. Over this same domain, the negative lengths rise to a maximum, but then, like the positive lengths, exhibit a gradual decrease out to $\epsilon y^+ \simeq 2.6$. On the figure, $y^+ = 40$ corresponds to 40ϵ, and therefore this position moves to the left with increasing δ^+. Thus, the profiles in figure 15(*b*) diverge at positions interior to $y^+ = 40$ in the $\delta^+ = 970$ flow. This is because the $\delta = 970$ flow has entered the inner scaling domain, while the $\delta^+ = 1500$ data are still in their intermediate scaling domain. As seen in figure 15(*b*), the minimum of the average lengths convincingly occurs at $\epsilon y^+ \simeq 2.6$.
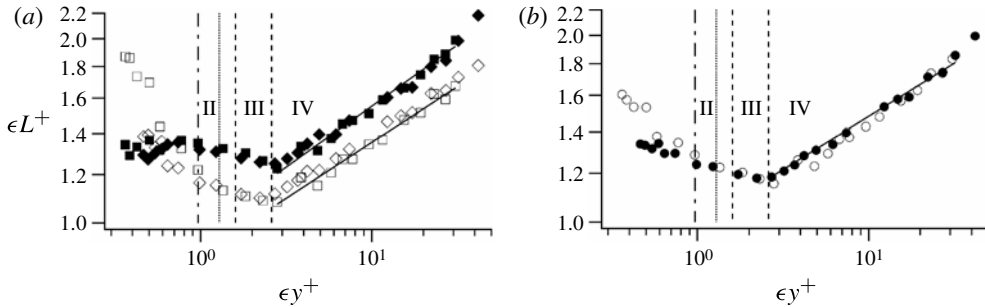
FIGURE 15. Streamwise lengths associated with ω_z. (*a*) Positive ω_z events: $\delta^+ = 970$ (□); $\delta^+ = 1500$ (◇); negative ω_z events: $\delta^+ = 970$ (■); $\delta^+ = 1500$ (◆). (*b*) Average of positive and negative event lengths: $\delta^+ = 970$ (○); $\delta^+ = 1500$ (●). Dashed lines denote layer III boundaries. Dotted line denotes 40ϵ at $\delta^+ = 970$. Dash-dot line denotes 40ϵ at $\delta^+ = 1500$.

The near-wall position where the L_p and L_n profiles cross is between $y^+ = 20$ and $y^+ = 25$. Beyond here, and into layer III, they develop a nearly constant difference that persists to $y^+ \simeq \delta^+$. Starting at $\epsilon y^+ \simeq 2.6$, the ω_z lengths exhibit an approximately power-law increase, although a logarithmic fit is also reasonable. The slope of the ϵL_n^+ line is observed to be slightly larger than the slope of the ϵL_p^+ line (0.20 versus 0.18). The ratios of the L_n/L_p profiles (not shown) indicate that for $\epsilon y^+ \gtrsim 2.6$, L_n maintains a slightly larger value than L_p for Reynolds numbers up to $\delta^+ \simeq 10^6$.

Taken together, the results of figure 14(*c–f*) support the depiction of vortical fissures in figure 3. The results of figure 14(*c–f*) also reinforce the spectral analyses of Morrill-Winter & Klewicki (2013), suggesting that $\sqrt{\nu\delta/u_\tau}$ is the characteristic scale at which the individual vortical motions organize at low Reynolds number, but at sufficiently high δ^+ (somewhere between $\delta^+ = 1500$ and $\delta^+ = 890\,000$) this scaling breaks down. In this regard, two possibilities are apparent: (i) the process occurs gradually over an extended δ^+ range; or (ii) the process occurs abruptly when a critical condition is met. Morrill-Winter & Klewicki (2013) suggest that the latter possibility, if it occurs, may be associated with a mixing transition akin to that described by Dimotakis (2000).

McKeon & Morrison (2007) have previously discussed the potential existence of a mixing transition in turbulent pipe flow. In addition, the study of Ishihara, Hunt & Kaneda (2011) reveals that high-Reynolds-number isotropic turbulence is characterized by embedded shear layers that contain a richly complex internal structure, and reinforce the results of Hunt *et al.* (2010, 2011) suggesting that thin internal shear layers are a generic element of high-Reynolds-number turbulence. The particle image velocimetry (PIV) measurements by Morris *et al.* (2007) provide evidence that the vortical fissures in a $\delta^+ \simeq 5 \times 10^5$ boundary layer are akin to shear layers, but have a complex internal structure. Thus, while the results of figure 14(*c,d*) are in accord with the physical processes indicated in figure 10, these processes apparently have added complexity associated with the ϵT^+ and ϵL^+ at $\delta^+ \simeq 890\,000$ being significantly smaller than those at low δ^+. The emergence of fine structure within the fissures provides a plausible explanation.

Estimates for the widths of the vortical fissures, Δ_f, as a function δ^+ were determined by taking a sample of transverse slices through the layer IV PIV vorticity contour measurements of Meinhart & Adrian (1995), Adrian *et al.* (2000) and Morris *et al.* (2007). These are the measurements that these researchers used to exemplify the properties of the fissures, and the (nominally) uniform-momentum zones that reside
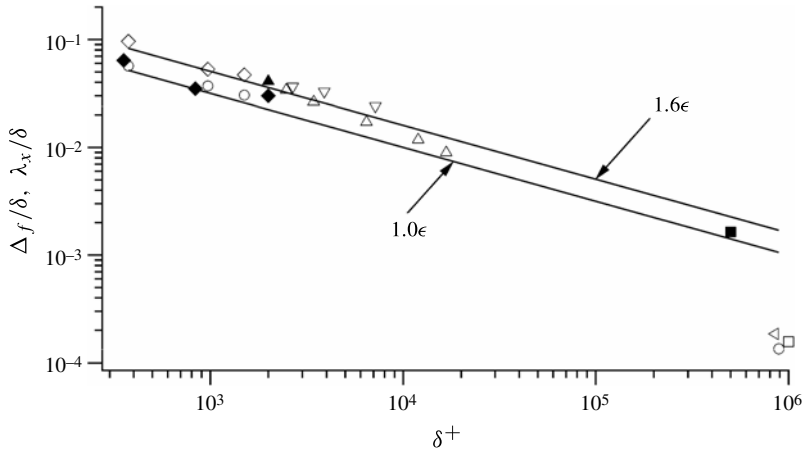
FIGURE 16. Vortical fissure thickness estimates normalized by δ versus δ^+: Meinhart & Adrian (1995) (▲); Adrian *et al.* (2000) (◆); Morris *et al.* (2007) (■). Streamwise Taylor microscale at $\epsilon y^+ = 2.6$: Klewicki & Falco (1990) (◇); Stanislas, Perret & Foucaut (2008) (▽); Marusic & Adrian (2013) (△); Metzger (2006) (◁); Klewicki, Priyadarshana & Metzger (2008) (□). Average of the positive and negative ω_z length scales from figure 14 (○).

between them. The sample size for each δ^+ was between 10 and 20 measurements. At any given δ^+, however, the scatter of the measurements was relatively small, with the sample standard deviations ranging between 8% and 26% of the sample mean. As with the vorticity event lengths in figure 14, the present fissure width measurements would probably shift sightly upward or downward if a different threshold were used to construct the underlying vorticity contours. The Reynolds number variations of the measured Δ_f are, however, expected to be relatively insensitive to such factors.

The measured fissure widths as normalized by δ are the solid symbols in figure 16. As indicated in figure 10, the fissures are surmised to form between $y^+ \simeq 40$ and the outer edge of layer III ($\epsilon y^+ \simeq 2.6$). Thus, the Δ_f/δ data are expected to nominally range between the thickness of layer III and layer II, ϵ and 1.6ϵ, respectively (solid lines on figure 16). The other data on this figure are streamwise Taylor length scale measurements, λ_x/δ, at $\epsilon y^+ \simeq 2.6$, and the average of the $\epsilon L_p/\delta$ and $\epsilon L_n/\delta$ measurements from figure 14(*e,f*), which were also evaluated at $\epsilon y^+ \simeq 2.6$. The λ_x/δ data attributed to Marusic & Adrian (2013) are derived from the measurements of Hutchins *et al.* (2009). The $\delta^+ = O(10^6)$ data are derived from the SLTEST site in Utah's western desert. The data point attributed to Klewicki *et al.* (2008) is previously unpublished. It comes from the average of two λ_x measurements using the two single-wire sensors that were deployed along with the microphones of that study, see figure 2 of Klewicki *et al.* (2008). The measurement attributed to Metzger (2006) comes from an experiment involving a rake of single-wire sensors. As Metzger demonstrates, this measurement also shows very good agreement with the λ_x measurements derived from the data set of Priyadarshana & Klewicki (2004).

The results of figure 16 suggest that at low δ^+ both Δ_f/δ and λ_x/δ scale with ϵ. Classical scaling estimates indicate that λ_x/δ should scale with ϵ in the boundary layer, e.g. Tennekes & Lumley (1972). The present fissure width estimates also indicate an adherence to this scaling at least up to $\delta^+ = O(10^6)$, and thus this attribute is depicted in figure 3. On the other hand, this scaling breaks down for λ_x, and by $\delta^+ = O(10^6)$, λ_x is about one tenth Δ_f, or equivalently, about equal to $\epsilon/10$. Metzger (2006) was
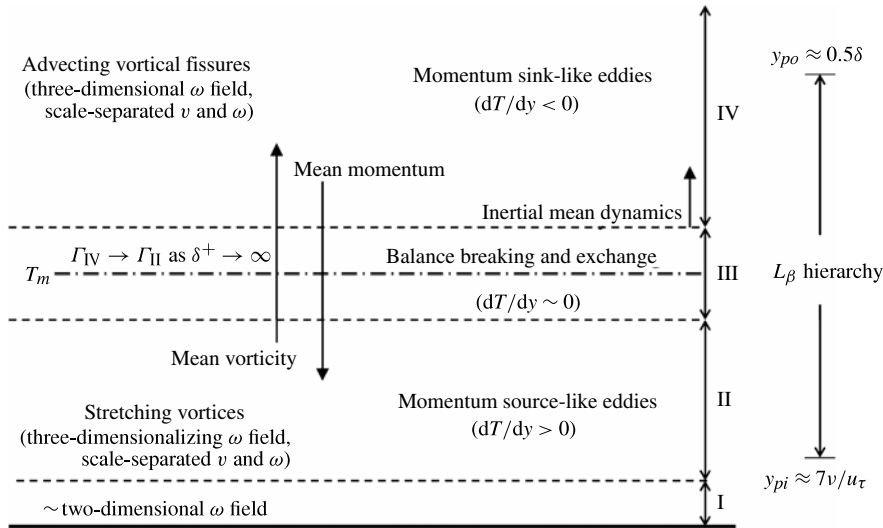
FIGURE 17. A physical model of the dynamical and vortical processes consistent with the mean similarity structure of turbulent wall-flow dynamics.

the first to provide a clear indication of this behaviour, and the present data reveal that this phenomenon also holds for the ω_z event lengths. This finding is similarly consistent with the result of Priyadarshana & Klewicki (2003) indicating that over the range $500 \lesssim \delta^+ \lesssim 1.5 \times 10^6$, spanwise vorticity frequency spectra merge when scaled by the Taylor time scale, λ_t. Similarly, Klewicki & Falco (1996) found that the present low $\delta^+ \omega_z$ event durations exhibit approximate invariance under normalization by λ_t. The results of figure 16 further suggest that at some relatively high δ^+ the fissures may begin to develop an intermittent internal structure. The λ_x/δ data of Marusic & Adrian (2013) provide a subtle indication that a more steeply downward trend in λ_x/δ may begin near $\delta^+ = 15\,000$.

At present, it seems safe to surmise that the overall velocity jump across each fissure is of primary importance when considering contributions to the mean velocity profile. The existence of a complex internal structure to the fissures may, however, prove to be important when considering how to modify boundary layer dynamics at high Reynolds number.

4. Discussion and conclusions

The vortical structure of turbulent wall flows was depicted in figure 3. Data pertaining to the vorticity field were then examined and scaled relative to the self-similar structure admitted by the mean dynamical equation. Discussions of the results relative to the depiction of figure 3 were given throughout, and thus are not repeated here.

Figure 17 presents a depiction of the mean dynamical structure by Klewicki *et al.* (2007), as updated with the vortical structure evidenced herein. It is considered to be a useful companion to figure 3. Features relevant to the mean dynamics are given on the right, while those associated with vorticity are on the left. The domain of the L_β layer hierarchy is represented on the far right. Across this hierarchy, the inertial turbulent motions span the full separation of scales, as reflected by $\delta^+ = \delta/(\nu/u_\tau)$. The flow

field mechanisms associated with the velocity–vorticity products in figures 2 and 13 are simultaneously responsible for the inward transport of momentum and the outward transport of vorticity depicted in the centre (Klewicki *et al.* 2007; Eyink 2008).

Interior to layer III, vorticity stretching, and to a lesser degree vorticity advection, characterize the momentum source-like motions. The spatial confinement mechanism for scale separation depicted in figure 3 stems from this vorticity stretching, as does the exchange from mean to fluctuating enstrophy, especially in the region $y^+ \lesssim 40$. Beyond layer III, vorticity advection, and to a lesser degree vorticity stretching, characterize the momentum sink-like motions. Here, scale separation occurs owing to the spatial dispersion of the vortical motions formed in layer II. This is also where the logarithmic mean profile emerges with increasing δ^+, as it is associated with the emerging linearity of the $W^+(y^+)$ profile, and thus $\phi \to \phi_c$ (Klewicki 2013*a*). This suggests that inner–outer interactions are embodied in the mechanisms that simultaneously sustain the two kinds of self-similarity (inner: $\phi \neq$ const., outer: $\phi = \phi_c$) associated with the invariant form admitted by (1.1). As discussed in greater length in the SM, the existing evidence suggests that the two mechanisms for scale separation are self-reinforcing via the inner–outer interactions across layer III.

Equation (1.3) describes the coordinate stretching that underlies the similarity solution admitted by (1.1). As in laminar flow, a knowledge of this coordinate stretching allows one to estimate the fraction of the flow volume occupied by the vorticity field as $\delta^+ \to \infty$ (Klewicki 2013*b*). A number of results pertaining to mean flow structure also relate to ϕ_c, while other empirically determined behaviours shown herein exhibit apparent dependence on this parameter. Given that ϕ describes how the average scale of the motions responsible for turbulent momentum transport are stretched to 'fit' within the physical space of the flow, it also seems worth noting that $\Delta_\mathrm{I}^+ \simeq \phi_c^2$, $\epsilon \Delta_\mathrm{II}^+ \simeq \phi_c$, and $\epsilon \Delta_\mathrm{III}^+ \simeq \phi_c^2 - \phi$. On-going efforts are being devoted to constructing well-founded explanations that clarify these observations.

Acknowledgements

Supplementary Data

Supplementary Material (additional data, their analysis and interpretation) are available at http://dx.doi.org/10.1017/jfm.2013.565.

REFERENCES

ABE, H, KAWAMURA, H. & MATSUO, Y. 2004 Surface heat-flux fluctuations in a turbulent channel flow up to $Re_\tau = 1020$ with $Pr = 0.025$ and 0.71. *Intl J. Heat Fluid Flow* **25**, 404–419.

ADRIAN, R. J., MEINHART, C. D. & TOMKINS, C. D. 2000 Vortex organization in the outer region of the turbulent boundary layer. *J. Fluid Mech.* **422**, 1–54.

CHENG, C. 2011 Numerical study of internal wall-bounded turbulent flows. PhD thesis, University of Melbourne, Victoria, Australia.

COLES, D. E. 1956 The law of the wake in turbulent boundary layers. *J. Fluid Mech.* **1**, 191–226.

DIMOTAKIS, P. E. 2000 The mixing transition in turbulent flows. *J. Fluid Mech.* **409**, 69–98.

ELSNAB, J., KLEWICKI, J., MAYNES, D. & AMEEL, T. 2011 Mean dynamics of transitional channel flow. *J. Fluid Mech.* **678**, 451–481.

EYINK, G. 2008 Turbulent flow in pipes and channels as cross-stream 'inverse cascades' of vorticity. *Phys. Fluids* **20**, 125101.

FIFE, P., KLEWICKI, J., MCMURTRY, P. & WEI, T. 2005a Stress gradient balance layers and scale hierarchies in wall-bounded turbulence. *J. Fluid Mech.* **532**, 165–189.

FIFE, P., KLEWICKI, J., MCMURTRY, P. & WEI, T. 2005b Multiscaling in the presence of indeterminacy: wall-induced turbulence. *Multiscale Model. Simul.* **4**, 936–959.

FIFE, P., KLEWICKI, T. & WEI, 2009 Time averaging in turbulence settings may reveal an infinite hierarchy of length scales. *J. Discrete Continuous Dyn. Syst.* **24**, 781–807.

HOYAS, S. & JIMENEZ, J. 2006 Scaling the velocity fluctuations in turbulent channels up to $Re_\tau = 2003$. *Phys. Fluids* **18**, 011702.

HUNT, J. C. R., EAMES, I., DA SILVA, C. B & WESTERWEEL, J. 2011 Interfaces and inhomogeneous turbulence. *Phil. Trans. R. Soc. Lond.* A **369**, 811–832.

HUNT, J. C. R., EAMES, I., WESTERWEEL, J., DAVIDSON, P. A., VOROPAYEV, S., FERNANDO, J. & BRAZA, M. 2010 Thin shear layers – the key to turbulence structure? *J. Hydro-environmental Res.* **4**, 75–82.

HUTCHINS, N., NICKLES, T. B., MARUSIC, I. & CHONG, M. S. 2009 Hot-wire spatial resolution issues in wall-bounded turbulence. *J. Fluid Mech.* **635**, 103–136.

ISHIHARA, T., HUNT, J. C. R. & KANEDA, Y. 2011 Conditional analysis near strong shear layers in DNS of isotropic turbulence at high Reynolds number. *J. Phys.: Conf. Ser.* **318**, 042004.

VON KÁRMÁN, T. 1930 Mechanische Ahnlichkeit und Turbulenz. *Nachr. Ges. Wiss. Göttingen, Math-Phys. Klasse* 155–162.

KLEWICKI, J. 2010 Reynolds number dependence, scaling, and dynamics of turbulent boundary layers. *Trans. ASME: J. Fluids Engng* **132**, 094001.

KLEWICKI, J. C. 2013a Self-similar mean dynamics in turbulent wall-flows. *J. Fluid Mech.* **718**, 596–621.

KLEWICKI, J. C. 2013b On the singular nature of turbulent boundary layers. *Proc. IUTAM*, Procedia IUTAM 9, 69–78.

KLEWICKI, J., CHIN, C., BLACKBURN, H., OOI, A. & MARUSIC, I. 2012 Emergence of the four layer dynamical regime in turbulent pipe flow. *Phys. Fluids* **24**, 045107.

KLEWICKI, J., EBNER, R. & WU, X. 2011 Mean dynamics of transitional boundary-layer flow. *J. Fluid Mech.* **682**, 617–651.

KLEWICKI, J. C. & FALCO, R. E. 1990 On accurately measuring statistics associated with small-scale structure in turbulent boundary layers using hot-wire probes. *J. Fluid Mech.* **219**, 119–142.

KLEWICKI, J. C. & FALCO, R. E. 1996 Spanwise vorticity structure in turbulent boundary layers. *Intl J. Heat Fluid Flow* **17**, 363–376.

KLEWICKI, J., FIFE, P. & WEI, T. 2009 On the logarithmic mean profile. *J. Fluid Mech.* **638**, 73–93.

KLEWICKI, J., FIFE, P., WEI, T. & MCMURTRY, P. 2007 A physical model of the turbulent boundary layer consonant with mean momentum balance structure. *Phil. Trans. R. Soc. Lond.* A **365**, 823–839.

KLEWICKI, J. C., MURRAY, J. A. & FALCO, R. E. 1994 Vortical motion contributions to stress transport in turbulent boundary layers. *Phys. Fluids* **6**, 277–286.

KLEWICKI, J. C., PRIYADARSHANA, P. J. A. & METZGER, M. M. 2008 Statistical structure of the fluctuating wall pressure and its in-plane gradients at high Reynolds number. *J. Fluid Mech.* **609**, 195–220.

LAADHARI, F. 2002 On the evolution of maximum turbulent kinetic energy production in a channel flow. *Phys. Fluids* **14**, L65–L68.

LIGHTHILL, M. J. 1963 Boundary layer theory. In *Laminar Boundary Layers* (ed. L. Rosenhead), Oxford University Press.

LIGHTHILL, M. J. 1958 On displacement thickness. *J. Fluid Mech.* **4**, 383–392.

MARUSIC, I. & ADRIAN, R. J. 2013 The eddies and scales of wall turbulence. In *Ten Chapters in Turbulence* (ed. P. Davidson, Y. Kaneda & K. R. Sreenivasan), Cambridge University Press.

MARUSIC, I., MONTY, J., HULTMARK, M. & SMITS, A. 2013 On the logarithmic region in wall turbulence. *J. Fluid Mech.* **716**, R3.

MCKEON, B. J. 2003 High Reynolds number turbulent pipe flow. PhD thesis, Princeton University, Princeton, New Jersey.

McKeon, B. J. & Morrison, J. F. 2007 Asymptotic scaling in turbulent pipe flow. *Phil. Trans. R. Soc. Lond.* A **365**, 771–787.

Meinhart, C. & Adrian, R. J. 1995 On the existence of uniform momentum zones in a turbulent boundary layers. *Phys. Fluids* **7**, 694–696.

Mellor, G. L. 1972 The large Reynolds number asymptotic theory of turbulent boundary layers. *Intl J. Engng Sci.* **10**, 851–873.

Metzger, M. 2006 Length and time scales of the near-surface axial velocity in a high Reynolds number turbulent boundary layer. *Intl J. Heat Fluid Flow* **27**, 534–541.

Metzger, M. M. & Klewicki, 2001 A comparative study of near-wall turbulence in high and low Reynolds number boundary layers. *Phys. Fluids* **13**, 692–701.

Monty, J. P. 2005 Developments in smooth wall turbulent duct flow. PhD thesis, University of Melbourne, Victoria, Australia.

Morrill-Winter, C. & Klewicki, J. 2013 Influences of boundary layer scale separation on the vorticity transport contribution to turbulent inertia. *Phys. Fluids* **25**, 015108.

Morris, S. C., Stolpa, S. R., Slaboch, P. E. & Klewicki, J. C. 2007 Near-surface particle image velocimetry measurements in a transitionally rough-wall atmospheric boundary layer. *J. Fluid Mech.* **580**, 319–338.

Nagib, H., Chauhan, K. & Monkewitz, P. 2007 Approach to an asymptotic state for zero pressure gradient turbulent boundary layers. *Phil. Trans. R. Soc. Lond.* A **365**, 755–770.

Oweis, G. F., Winkel, E. S., Cutbrith, J. M., Ceccio, S. L., Perlin, M. & Dowling, D. R. 2010 The mean velocity profile of a smooth-flat-plate turbulent boundary layer at high Reynolds number. *J. Fluid Mech.* **665**, 357–381.

Perry, A. & Chong, M. 1982 On the mechanism of wall turbulence. *J. Fluid Mech.* **119**, 173–217.

Perry, A., Henbest, S. & Chong, M. 1986 A theoretical and experimental study of wall-turbulence. *J. Fluid Mech.* **165**, 163–199.

Perry, A. & Marusic, I. 1995 A wall-wake model for the turbulence structure of boundary layers. Part 1. Extension of the attached eddy hypothesis. *J. Fluid Mech.* **298**, 361–388.

Priyadarshana, P. J. A. & Klewicki, J. C. 2003 Reynolds number scaling of wall layer velocity-vorticity products. In *Reynolds Number Scaling in Turbulent Flow* (ed. A.J. Smits), pp. 117–123. Kluwer Academic Publishers.

Priyadarshana, P. J. A. & Klewicki, J. C. 2004 Study of the motions contributing to the Reynolds stress in high and low Reynolds number turbulent boundary layers. *Phys. Fluids* **16**, 4586–4600.

Priyadarshana, P. J. A., Klewicki, J. C., Treat, S. & Foss, J. F. 2007 Statistical structure of turbulent-boundary layer velocity-vorticity products at high and low Reynolds numbers. *J. Fluid Mech.* **570**, 307–346.

Sayadi, T., Hamman, C. W. & Moin, P. 2013 Direct numerical simulation of complete H-type and K-type transitions with implications for the dynamics of turbulent boundary layers. *J. Fluid Mech.* **724**, 480–509.

Schlatter, P. & Orlu, R. 2010 Assessment of direct numerical simulation data of turbulent boundary layers. *J. Fluid Mech.* **659**, 116–126.

Stanislas, M., Perret, L. & Foucaut, J. M. 2008 Vortical structures in the turbulent boundary layer: a possible route to a universal representation. *J. Fluid Mech.* **602**, 327–382.

Tennekes, H. & Lumley, J. 1972 *A First Course in Turbulence*. MIT.

Townsend, A. 1976 *The Structure of Turbulent Shear Flow*. Cambridge University Press.

Wei, T., Fife, P., Klewicki, J. & McMurtry, P. 2005 Properties of the mean momentum balance in turbulent boundary layer, pipe and channel flows. *J. Fluid Mech.* **522**, 303–327.

Wosnik, M., Castillo, L. & George, W. K. 2000 A theory for turbulent pipe and channel flows. *J. Fluid Mech.* **421**, 115–145.

Wu, X. & Moin, P. 2008 A direct numerical simulation study on the mean velocity characteristics in turbulent pipe flow. *J. Fluid Mech.* **608**, 81–112.

Wu, X. & Moin, P. 2009 Direct numerical simulation of turbulence in a nominally zero-pressure-gradient flat-plate boundary layer. *J. Fluid Mech.* **630**, 5–41.

Yajnik, K. S. 1970 Asymptotic theory of turbulent shear flows. *J. Fluid Mech.* **42**, 411–427.